An automatic planning method for breast electronic tissue compensation treatments based on breast radius and separation

by

Alexander Rudolf Podgorsak
May 2020

A thesis submitted to the
Faculty of the Graduate School of
the University at Buffalo, The State University of New York
in partial fulfillment of the requirements for the
degree of

Master of Science

Medical Physics Progam
Department of Radiology

Acknowledgement

Foremost, I would like to thank my project advisor Dr. Lalith Kumaraswamy for all of his time throughout this project. I went to pester him many times during the past two years with questions, and was not turned back a single time. I am grateful for his professional and personal advice throughout my academic career. Good luck at the new institute!

Additionally, I would like to thank my co-advisor Dr. Ciprian N. Ionita for his helpful feedback along the way and for affording me the flexibility to work on this project on the side as I work towards a PhD in his group.

Lastly and certainly not least, I would like to thank my family for the love and support they have showed me. To my Mom, for putting up with many a technical discussion at the dinner table over the years. To my Dad, for instilling in me a passion for Medical Physics from a young age. To my siblings, for putting up with my occasionally cantankerous mood as this project has taken shape. To Grizzly, for never caring how slow the project progress was and always acting excited to see me.

Table of Contents

List of Figures

Page

List of Tables

Page

List of Equations

Page

Abstract

One of the techniques used for breast radiation therapy employs two electronically compensated tangent fields. This technique has been shown to minimize irradiation of the surrounding pulmonary and cardiac tissue, while improving the homogeneity of the delivered dose within the breast volume. Much work has been carried out to correlate the size and shape of the breast, defined by breast radius and separation, with the amount of tissue compensation needed to deliver the most homogenous dose distribution. These methods so far have assumed either a single or three radius and separation measurements throughout the breast volume (called the one- and three-region breast model), instead of accounting for the variation in radius and separation in the cranio-caudal direction. We developed a semi-supervised algorithm to determine the size and shape of the breast at each axial location using the pre-treatment CT-simulation image data, and correlate it to the optimal level of tissue compensation. Ten treatment plans generated in this manner were compared with the original medical dosimetrist plans for the dose homogeneity throughout the breast volume and for conformity to institutional dose constraints. Additional comparisons were with plans generated using the one- and three-region breast models.

We measured statistically non-inferior dose homogeneity from plans generated from our automated framework compared with the medical dosimetrist plans over the collected courses. Additionally, our framework's plans improved on dose homogeneity compared with plans generated using the one- and three-region breast model, indicating that considering the variation in the breast radius and separation in the cranio-caudal direction improves the treatment plans. Compared with the medical dosimetrist plans, our

automated algorithm requires much less user input and generates plans in an average of 20 seconds compared with the 30 minutes of full attention it can take a dosimetrist.

This work indicates the potential clinical utility for an automated technique for the generation of more homogenous breast electronic compensation treatment plans compared with a one- or three-region breast model. We envision this process attaining a more consistently homogenous starting point for further optimization by the medical dosimetrist compared with the current standard starting point one-region breast model.

Chapter 1: Introduction of Basic Concepts

1.1 – Breast Cancer

1.1.1 – Incidence and Statistics

Breast cancer is a problem of great clinical significance to women in the United States. According to the American Cancer Society and National Cancer Institute[1], about 1 in 8 U.S. women will develop invasive breast cancer over the course of her lifetime[2]. In 2020, an estimated 276,480 new cases of invasive breast cancer (Figure 1) and 48,530 new cases of non-invasive breast cancer are expected to be diagnosed. 42,170 women in the U.S. are expected to die in 2020 from breast cancer, and for women in the U.S., breast cancer death rates are higher than those for any other cancer save for lung cancer (Figure 1). As of January of 2020, there are more than 3.5 million women with a history of breast cancer in the U.S., including those women currently being treated and those who have completed treatment. Save for skin cancer, breast cancer will be the most commonly diagnosed cancer among American women. In 2020, it is estimated that 30% of newly diagnosed cancers in women will be breast cancer. All of this being said, the 5- and 10-year relative survival rates for women with

Estimated New Cases

Breast	276,480	30%
Lung & bronchus	112,520	12%
Colon & rectum	69,650	8%
Uterine corpus	65,620	7%
Thyroid	40,170	4%
Melanoma of the skin	40,160	4%
Non-Hodgkin lymphoma	34,860	4%
Kidney & renal pelvis	28,230	3%
Pancreas	27,200	3%
Leukemia	25,060	3%
All sites	**912,930**	

Estimated Deaths

Lung & bronchus	63,220	22%
Breast	42,170	15%
Colon & rectum	24,570	9%
Pancreas	22,410	8%
Ovary	13,940	5%
Uterine corpus	12,590	4%
Liver & intrahepatic bile duct	10,140	4%
Leukemia	9,680	3%
Non-Hodgkin lymphoma	8,480	3%
Brain & other nervous system	7,830	3%
All sites	**285,360**	

Figure 1: 2020 estimates of leading sites of new invasive cancer and deaths for American women. Breast cancer statistics highlighted. Statistics from the American Cancer Society.

invasive breast cancer are 91% and 84% respectively. If the cancer is caught at a localized stage before it spreads to the lymphatic system, the 5-year survival rate is 99%.

1.1.2 – Detection

As mentioned in the previous subsection, detecting breast cancer in its localized stage is essential to maximize the patient's survival rate. Image-based screening for breast cancer using mammography is widespread. It is estimated that 65.3% of women aged 40 or older have undergone a mammogram since the year 2018[3]. Mammography is a low-dose planar x-ray imaging procedure that can visualize early signs of breast cancer prior to the onset of symptoms. Traditionally, this was a modality which used radiographic film for image visualization, recent times have brought about digital mammography[4]. It is undeniable that mammography aids in the early detection of breast cancer, but questions persist regarding the proper screening schedules and the appropriate age at which women should start regular screening[5]. The American Cancer Society recommends women begin regular mammographic screening starting at age 45, but this can depend on other risk factors such as family history. Concerns of radiation-induced breast cancer due to the dose delivered from years' worth of mammograms are reported[6], as well as the cost and potential patient discomfort during the mammography procedure are reasons many women resist regular mammography screening. These concerns have led to much research regarding other methods for breast cancer screening such as with magnetic resonance imaging (MRI)[7] or ultrasound[8]. Additionally, mammography is limited in that all of the volumetric information is integrated over the axial direction, which may inhibit proper appreciation of any early signs of breast cancer. These concerns have led to the development of breast tomosynthesis techniques, which can acquire volumetric

information regarding the breast[9]. This increase in information available to clinicians has been reported to aid in the early detection of breast cancer[10].

Following a positive finding from initial screening, a woman will typically undergo a surgical biopsy procedure, where a tissue sample from the breast will be extracted and sent for further investigation[11] to determine the staging and subtype of the disease. Following this, if the positive disease state is confirmed, the treatment course will be determined depending on the disease stage and cancer subtype.

1.1.3 – Treatment Options

As mentioned in the previous subsection, treatments for breast cancer will depend on the specific tumor subtype categorized according to the presence of estrogen or progesterone receptor expressions[2]. Typically, there will be some combination of hormone therapy along with the delivery of chemotherapy drugs to the tumor site for patients with the receptor-positive tumors. These chemotherapy drugs are preferentially taken in by the rapidly dividing tumor cells, leading to their death via RNA or DNA damage interrupting the cell division process[12]. Targeted antibodies are also being used[13] for a more precise and accurate delivery of the treatment to the tumor, which may reduce some of the associated toxicity from chemotherapy[14]. For patients with receptor negative tumors, which is reported to have a poorer prognosis compared with the receptor positive subtypes[15], a lumpectomy or even total mastectomy may be considered. In the case of surgical removal of some or the entire breast, it is typically performed in-conjunction with post-surgical radiation therapy[16], either using an external x-ray beam or with implantation of radiation-delivery devices in the breast (brachytherapy) near the site. This is done to ensure that tumor cells that may have extended to surrounding tissue are killed such that

the chance of disease recurrence is reduced. This killing action of the radiation source is due to either direct damage to the tumor cell's DNA or other molecules, or indirect damage following the production of hydroxyl free-radicals[17]. It is important to note that treatments such as surgery and radiation therapy are called local treatments, compared with chemotherapy, which is called a systemic treatment. Surgery and radiation therapy target one location of the body (ignoring potential side effects of the therapies), whereas chemotherapy drugs will travel throughout the body and affect cells far from the primary tumor.

1.2 – Radiation Therapy for Breast Cancer

1.2.1 – Brachytherapy

Brachytherapy is the delivery of radiation to a target with an implanted radiation source, either temporary or permanent. Brachytherapy techniques for breast cancer treatment typically use a high-dose rate radiation source[18] that is temporarily implanted to the target site, then retracted following delivery of the prescription dose. The use of breast brachytherapy following either a lumpectomy or a mastectomy has increased in recent years[19] as an alternative treatment method to whole-breast irradiation with an external radiation beam. Compared with whole-breast irradiation, it is reported that brachytherapy leads to less breast tissue irradiation and requires a shorter treatment course[20]. This smaller more targeted treatment volume may lead to insufficient residual tumor killing, causing more disease recurrence potentially necessitating further surgical intervention such as a mastectomy[21]. It is reported that in specific cohorts, brachytherapy compared with whole-breast external beam irradiation results in worse breast preservation and increased complications, but no difference in patient survival[19]. The associated risks with

the increase in brachytherapy post-procedural complications have not yet been quantified.

1.2.2 – External Beam Whole Breast Irradiation

It is reported that women who undergo lumpectomy followed by whole-breast external beam irradiation for breast cancer treatment have a reduced risk for disease recurrence which may prevent the need for an eventual mastectomy[22-25]. This treatment modality delivers dose with an external x-ray beam, generated in the present day with a linear accelerator (LINAC). External beam radiotherapy for breast cancer treatment is carried out with two x-ray fields in the mega-volt peak (MV) beam energy range. These treatments are fractionated, meaning that the prescription dose is not given all at once – rather, daily radiation doses are administered which sum to the prescription dose which is typically around 40 Gy. These doses are typically administered over the course of more than a month. Without this fractionation scheme, the toxicity of the administered radiation to healthy tissue would be too great[26,27] and would outweigh any treatment benefits. This fractionation schedule is the topic of much current research, and there are studies which point to what might be the most optimal one defined by rate of disease recurrence and radiation-induced morbidity[28-30]. In many ways, a quicker, “hypofractionated” radiation-delivery schedule might be important from the standpoint of patient convenience. Hypofractionation is the delivery of the typical 40 Gy prescription dose with a larger daily dose to the target, administered over a shorter amount of time when compared with a normally-fractionated schedule. Radiobiological models suggest that such a delivery scheme could be just as effective[31] for treatment, while being more convenient for the patient when compared with a normally-fractionated radiation delivery schedule. This is

important, as it is reported that 30% of North American women forgo the radiation therapy following lumpectomy due, in part, because of the time and cost of the therapy[32].

1.3 – External Beam Radiation Therapy Breast Cancer Treatment Concerns

1.3.1 – Dose to Healthy Tissue

Similar to all applications of radiation therapy, the healthy tissue near the target site must be protected. The dose delivered to these healthy structures must be minimized to reduce the chances of radiotherapy-induced side-effects such as secondary cancers[33], and specific to cancer treatments near the heart, radiation-induced cardiomyopathy[34]. These concerns have a large clinical footprint, as 120,000 American women with breast cancer are treated annually with external beam radiotherapy[35-37]. To maximize the coverage of the treatment volume, while minimizing the potential negative impact on the healthy surrounding tissue, two tangentially opposed fields (180° apart, Figure 2) are used for radiation dose delivery. This type of beam geometry maximizes the radiation field coverage to irradiate the whole breast, while minimizing the dose to the ipsilateral lung and heart such that some of the radiation-associated toxicity of this treatment modality may be reduced. This is an important concept, as it is reported that women treated for breast cancer with external beam radiation therapy have a higher incidence of coronary artery disease and the previously mentioned myocardial infarction[38-40]. This two-field opposed tangential approach provides good local tumor control with a <1% local recurrence rate[41].

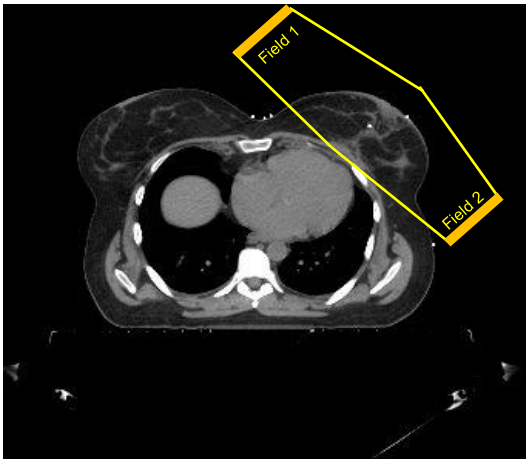

Figure 2: Axial CT-simulation slice with exemplification of tangentially opposed fields used for breast cancer treatment

1.3.2 – Homogenous Dose Delivery

An additional goal of external beam radiation therapy is to homogenously deliver the prescription dose throughout the entire treatment volume[42]. The standard two tangentially opposed field approach does not necessarily provide this[43]. It is challenging to achieve a homogenous delivery of the prescription dose throughout the entire breast volume due to the shape of the breast[44,45]. Organs such as the breast and the nose that have thinner and thicker regions due to curvature are often difficult locations to deliver a homogenous radiation dose. Attempting to achieve at least 95% of prescription dose in the treatment volume as is a standard institutional dose constraint will often lead to hotspots in the breast volume which may result in overdosing the breast, often measured as a dose some percentage over 100% of the prescription dose[46] depending on the specific institutional constraints. Improvement in the dose homogeneity has been shown to reduce the onset of adverse effects such as acute radiation toxicity and poor cosmetic outcomes, especially in women with large breast sizes[47,48]. Additionally, as more plans shift towards a hypofractionated approach, dose homogeneity becomes an even more important[49] consideration.

1.4 – Solutions to Improve Dose Homogeneity

1.4.1 – Intensity Modulation with Physical Wedge Filters

Wedge filters are used in external beam radiation therapy for different organs to improve the homogeneity of the delivered dose throughout the target volume[50]. The wedge filter causes a modulation in intensity across the beam resulting in a modification in the isodose lines, where the thicker end of the wedge causes a reduction in beam intensity beneath it (Figure 3)[51]. This can be desired in organs such as the breast, where the thicker portion of the wedge can be placed above the anterior portion of the breast, which is thinner than breast regions posterior. A wedge can prevent overdosing of these thinner regions and improve the homogeneity of the dose delivery throughout the entire breast treatment volume. Wedge filters are made of a material highly attenuating to x-rays such as lead or steel. The amount of tilt that the wedge will induce in the isodose curves is dependent on the slope of the wedge filter; a higher sloping filter will lead to more isodose line tilt, and vice-versa for a less sloping filter. The wedge that is selected is task- and patient-specific. In recent years, radiation beam intensity modulation with physical compensators including physical wedges have been superseded by dynamic multileaf collimators (MLC)[52-54] to go along with intensity-modulated radiation therapy (IMRT).

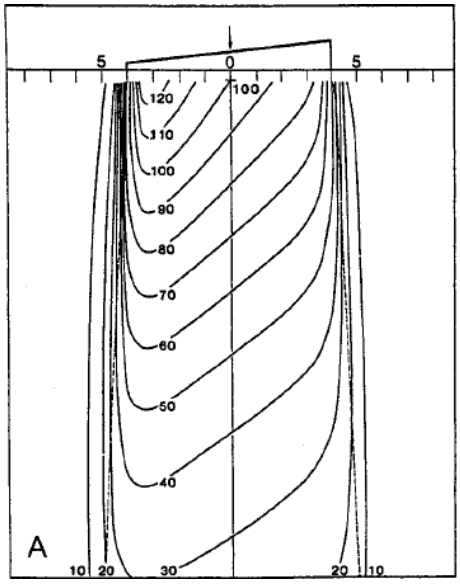

Figure 3: Isodose curves tilted to thinner edge of wedge filter.

1.4.2 – Intensity Modulation with MLC

The introduction of MLC beam intensity modulation to clinical practice has greatly improved the ability of the external-beam radiation therapy treatment planner to maximize the coverage of the treatment volume while minimizing the dose to peripheral healthy

tissues. Both of these factors lead to improved dose homogeneity within the treatment volume when compared with classical beam modulation techniques such as physical wedges, or treatments using no intensity modulation[55]. The MLC achieves this intensity modulation with the motion of individual tungsten “fingers” (Figure 4)[56] that move in and out of the radiation beam to shape the treatment area and modulate the fluence of the delivered radiation with time. The resolution of this intensity modulation is dependent on the spatial width of each of the collimator fingers, as well as how quickly they can be moved in and out of the beam. The MLC sits within the LINAC head and does not require any manual insertion or removal from treatment to treatment.

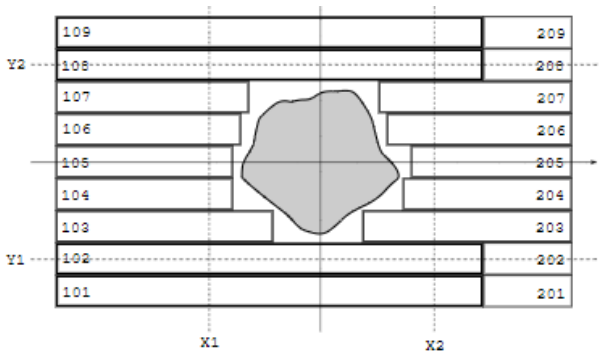

Figure 4: Conformal shaping of the delivered beam with the position of the multileaf collimator (MLC) fingers. Intensity modulation is achieved with dynamic motion of the MLC.

A specific approach to utilization of the power of IMRT in the context of breast cancer is electronic compensation of the tangential opposed radiation fields[57-59]. This technique uses dynamic motion of the MLC during the treatment to vary the beam fluence to more-homogenously deliver dose to the irregular breast volume. This irregular compensation surface can account for variation in breast thickness in both the anterior-posterior direction and cranio-caudal direction[60], which is a strength of this technique as the breast organ has much variation in those directions making it difficult for classical methods to deliver a homogenous dose distribution. The compensation surface is defined with a transmission penetration depth (TPD), which is the point along every ray within the x-ray field that the tissue compensation occurs. A TPD of 50% indicates that the compensation

surface is at the halfway point through the breast at each ray in the x-ray field. If the TPD is reduced, the compensation surface is moved closer to the radiation entry breast surface. If the TPD is increased, the opposite is true. This concept is shown in Figure 5. The homogeneity of the delivered plan is improved using electronic compensation through careful selection of the TPD.

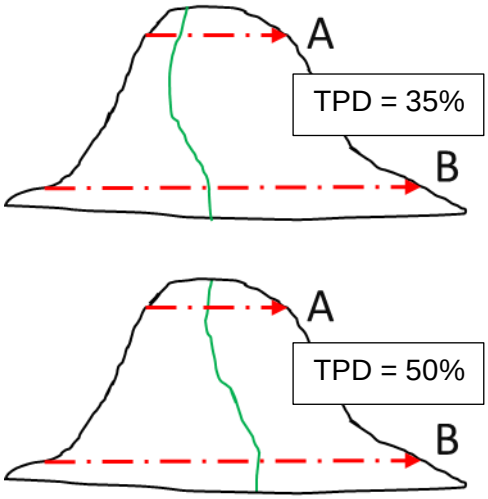

Figure 5: Outline of axial slice of asymmetric breast (black) with irregular compensation surface (green) for diverging field with beamlets A and B (red) detailing (top) TPD of 35% and (bottom) TPD of 50%.

Forward planning is conventionally used for electronic compensation breast cancer treatments, where a dose prescription and constraints are set, and a planner attempts to manually combine different beam configurations and MLC motion to suitably match the prescription and meet the institutional constraints with an iterative process. This is the reverse of inverse planning, where the dose prescription and constraints are set, and an algorithm is optimized such that the prescription and constraints are met through the selection of beam combinations and MLC motion. Inverse planning can be computationally intensive, and until recently has not made its way into clinical practice due to hardware restrictions[61], although that is starting to change in recent years with the advent of parallel computing and cheaper processing power[62].

A second consideration to these treatments is the x-ray beam energy selected for the tangentially opposed fields. At Roswell Park Comprehensive Cancer Center, either solely a 6 MV x-ray beam or a combination of a 6 MV and a 23 MV beam fractionally weighted is used depending on the size of the breast. The higher beam energy is sometimes

employed in cases of large breasts to better deliver the dose to the deeper portions of the breast without overdosing the surrounding tissue.

1.4.3 – Shortfalls of Current Methods

As mentioned in a previous subsection, electronic compensation is currently forward planned, typically by a medical dosimetrist. This means that the dosimetrist adjusts certain parameters manually in an iterative process until the dose prescription is met and any dose constraints are satisfied. Dose constraints that are typically set include minimum and maximum percentage of prescription dose to avoid radiation hot and cold spots in the treatment volume, as well as maximum radiation dose delivered to peripheral tissue and critical organs such as the ipsilateral lung and the heart. The TPD is one of the parameters that is tuned to adjust the delivered radiation fields. Clinically, the TPD is initialized based on prior knowledge of the treatment planner, and modified iteratively. The dose profiles are modified manually to reduce x-ray fluence in regions of hotspots, and increase x-ray fluence in regions of cold spots. This iterative process can be a time-consuming one, where meeting the entire plan constraints can take the dosimetrist tens of minutes, or even longer to achieve. Additionally, there can be large variability between different

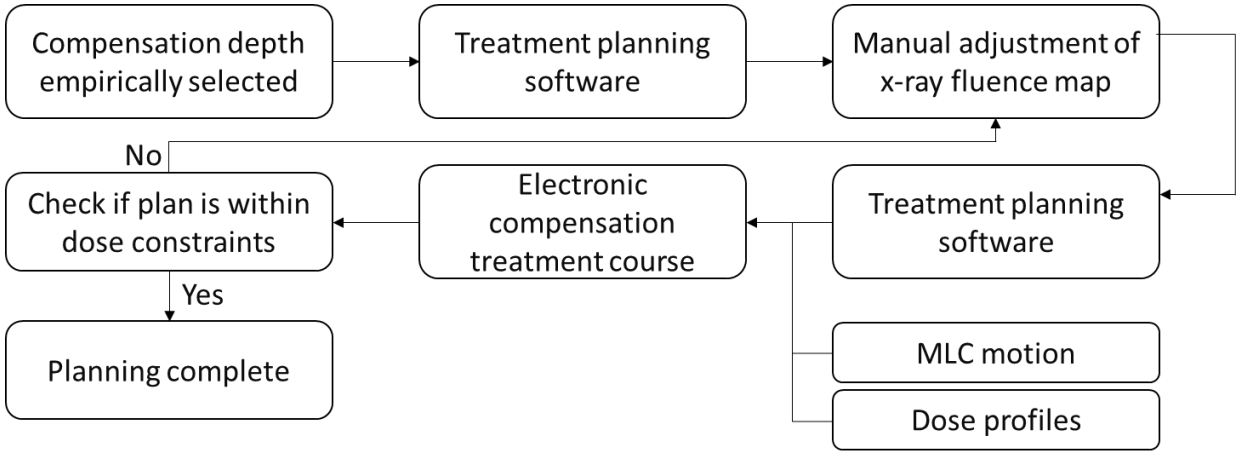

Figure 6: Flowchart exemplifying the current planning process for electronic compensation forward treatment planning. This forward planning is an iterative process that requires manual editing of the fluence map to bring the plans within institutional dose constraints.

treatment planners based on their experience and skill. This process may be contributing to some of the dosimetrist burnout reported in the literature[63]. The current clinical workflow is exemplified by the flowchart shown in Figure 6.

Work has been published which has attempted to automate certain portions of the electronic compensation forward planning, by correlating the size and shape of the breast to the TPD which yielded the most homogenous dose delivery. Friend and authors reported the use of a constant TPD rule depending of the breast separation, TPD 40% if the separation is greater than 24 cm, TPD of 50% otherwise[64]. Emmens and James reported the use of smaller TPD for breasts with larger maximum separation producing a more homogenous dose distribution, while also indicating that the entire breast volume should be taken into account to achieve the most homogenous dose distribution[65]. These works are an improvement over the manual iterations needed with the current clinical workflow, in that the treatment plans should satisfy the dose constraints quicker and with less manual input by the medical dosimetrist. However, they are not perfect. These works used a single TPD throughout the entire treatment volume, thus ignoring the variation in

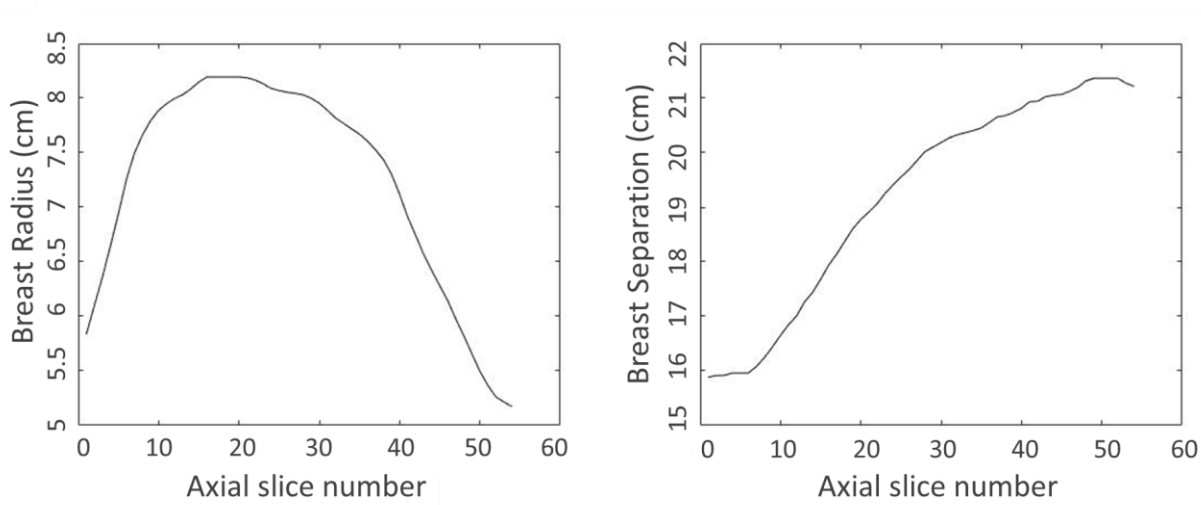

Figure 7: Left shows how the breast radius varies in the cranio-caudal direction; right shows how the breast separation varies in the cranio-caudal direction for the same collected patient breast.

breast size in the cranio-caudal direction. Figure 7 shows an example of how the breast radius and separation may vary in the cranio-caudal direction. It seems likely that there is additional dose homogeneity that can be recovered through considering more of this information when treatment planning. Alghufaili and colleagues correlated the entire contour of the breast to the optimal TPD to the end of achieving a homogenous dose delivery[66]. This work broke the breast into three discrete regions (superior, middle, inferior), and using the average radius and separation in each of the regions output treatment plans using three separate TPDs in the cranio-caudal direction.

1.5 – Proposed Work

Our work looks to build on the works of Friend and colleagues, Emmens and James, and Alghufaili and colleagues, in that the entire breast size and shape at each axial slice will be used to determine the optimal TPD for the treatment plan. Each ray within the tangentially opposed fields will have a different TPD based on the variation in the breast radius and separation in the cranio-caudal direction, and this work will account for this. Figure 8 shows an exemplification of how our work may improve on previous attempts of correlating TPD to the breast size and shape. Attempting to select a single or a few TPDs which is optimal over the entire breast volume is impossible due to the variation in breast size and shape. It seems likely that improvements in the dose

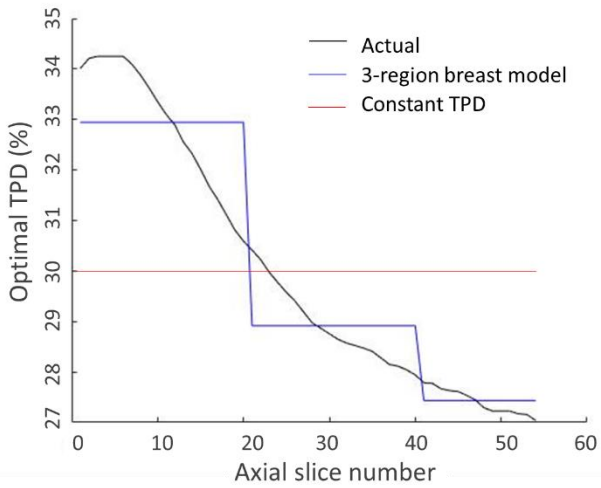

Figure 8: Actual optimal compensation depth (TPD) as a function of axial slice and two proposed models for optimal TPD.

homogeneity with the electronic compensation technique may be realized with a higher-resolution correlation of breast size and shape to the optimal x-ray fluence. We look to do this optimal TPD selection with a completely automated and comprehensive framework, such that both the variation in plans across different treatment planners may be mitigated, and the manual input required of the medical dosimetrist may be reduced. This work can be broken up into two portions. Firstly, an automated measurement technique must be developed which can accurately assess the breast size and shape using already clinically acquired pre-treatment imaging as the sole input. Secondly, the result of this size and shape measurement must be correlated to the proper beam fluence such that the delivered dose profile is optimally homogenous. We consider this work as a potentially better starting point for the forward planning procedure of the medical dosimetrist. Instead of starting with a plan obtained using an empirically determined TPD, requiring many iterations and lots of manual input to satisfy dose constraints, an automated framework such as our proposed algorithm could be used which may only require minimal modification prior to treatment.

Chapter 2: Automatic Measurement of Breast Radius and Separation

2.1 – Pre-treatment imaging

There has been a bevy of research into radiation therapy planning with imaging modalities such as MRI[67], but conventional electronic compensation techniques are proceeded by CT-based imaging for target delineation and healthy structure localization[68,69]. Additionally, the attenuation data that CT provides is crucial for dose delivery estimation during the treatment planning stage. Volumetric imaging allows for the computation of three-dimensional dose calculations during treatment planning which provides the most accurate simulation of the prescribed treatment. The image data from the CT-simulation is first used for segmentation and definition of not only the treatment volume but also the surrounding healthy tissue and structures including the lung volume and heart. A radiation oncologist typically carries out this segmentation process manually, but much recent work has been carried out regarding the automatic segmentation of structures utilizing artificial intelligence and machine learning[70,71]. If certain structures like the lung or heart are in danger of radiation-induced damage due to the treatment, additional dose constraints can be applied to the treatment to avoid the damage.

2.2 – Breast Size Measurement Algorithm Development

2.2.1 – Ground Truth Data

CT-simulation imaging is carried out as part of the standard pre-treatment clinical workflow at Roswell Park Comprehensive Cancer Center, hence it makes sense to use this type of imaging as the input to the automatic breast size and shape algorithm. To this end, we retrospectively collected and anonymized three patients' CT-simulation data to

develop the automated framework for measurement of the breast radius and separation. These were patients who were undergoing electronically compensated whole-breast external beam radiation therapy for breast cancer treatment. Informed consent was waived, as this was a retrospective collection of patient image data. Included in this small collection of patient data were two left-sided and one right-sided treatment. To assess the accuracy of the proposed automated breast size measurement tool, ground truth measurements were performed by hand in each axial slice in the treatment volume of the three collected patient datasets. In these cases, the treatment volume was determined by placement of superior and inferior platinum markers on the patient prior to simulation. The two measurements that typically define the breast size and shape in the literature are the breast radius and separation. In this work, we defined the breast radius as the distance from the chest wall to the anterior apex of the breast, and the breast separation as the distance along the posterior edge of the breast. Figure 9 details the breast radius and separation measurement methods used in this work.

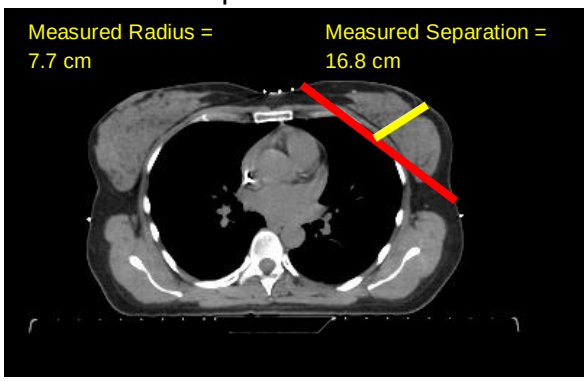

Figure 7: Left breast radius (yellow) and separation (red) hand-measurement with result overlaid on figure. This process was repeated for each axial slice in three patients' treatment volumes.

2.2.2 – Image Pre-processing

Our algorithm was developed within MATLAB R2016a (MathWorks, Massachusetts, USA). The first step of our framework is the identification of medial and ipsilateral platinum markers placed prior to CT-simulation. It is important that these markers are platinum, as it makes for easy identification from the rest of the image data using simple intensity thresholding. Platinum is highly attenuating to x-rays (Z=78) and these markers will have the highest intensity in CT-simulation image data save for certain image artifacts. Two square ROIs are required as input to the algorithm (Figure 10), the first is around the ipsilateral marker and the second around the medial marker. These ROIs can be rather large, and just roughly localize the markers to the algorithm such that any artifacts which may be present in the image data do not corrupt the algorithm. Within each of the two ROIs, the pixel location with the highest intensity is determined to be the marker location. If the medial marker is found to be to the right of the ipsilateral marker by x-position, the treatment is a left-sided treatment, otherwise if the medial marker is to the right of the ipsilateral marker, it is a right-sided treatment. A vector is created connecting the two marker coordinates, extrapolated out to the image boundaries (Figure 11), and all structure beneath this vector is

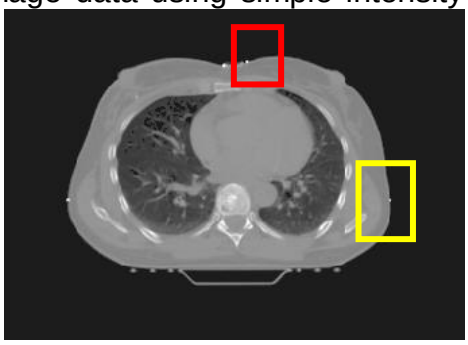

Figure 10: Example of ROI selection for left-sided breast ipsilateral (yellow) and medial (red) identification.

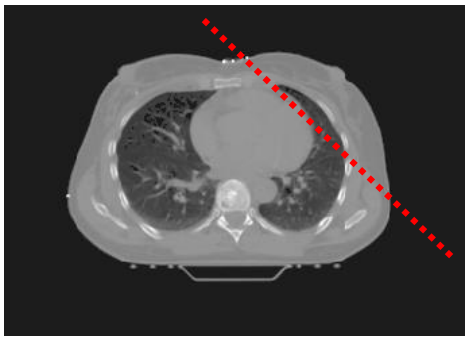

Figure 11: Vector connecting ipsilateral and medial markers following identification with intensity thresholding.

Figure 12: Removal of image data beneath vector leaving just the targeted breast at specific axial slice.

removed from the image data (Figure 12). There is one last removal of spurious structures in the image data with a morphological opening operation[72]. This removes small structures and other noise that may have been in the image data. The intent of these pre-processing steps is to remove all of the image data that is not the targeted breast, to simplify the anatomy for the breast radius and separation estimation. Structures like the patient couch and other patient anatomy could potentially confound the algorithm and add more complexity to the breast radius and separation estimation.

2.2.3 – Hough Transform

Initially developed for analysis of lines within bubble chamber photographs[73], the Hough transform is a feature extraction technique with widespread usage in computer vision and image processing[74]. Extended to the detection of arbitrary shapes in 1981 by Ballard with template matching[75], the Hough transform is a popular technique for the identification of the positions, contours, and orientation of ellipses and circles[76].

In the case of circle detection, there are three parameters that must be identified for a well-detected shape; the x and y coordinate of the center of the circle and the circle's radius. These three parameters are determined through a voting procedure carried out in the two-dimensional parameter space of the circle's center coordinates, and the one-dimensional parameter space of the circle's radius. In each of the parameter spaces, the highest voted circle center and radius will be the local maxima and can therefore be detected and re-mapped to the original image for circle detection. The circular Hough transform has been utilized for widespread applications such as automatic people counting detecting heads and circles[77], and in the context of brain aneurysm detection and classification from digital subtraction angiography image data[78]. More detail

regarding the operation of the Hough transform for a generalized circle identification will follow.

A generalized Hough transform typically beings with some form of edge-detection. This edge-detection can be a simple one such as the Sobel-Feldman operator[79], which is the use of two 3x3 convolutional kernels applied to the image data to compute horizontal and vertical gradients. The result of this is a two-dimensional map of the gradient at each point. Areas of high gradient will be highly visible in the output as white lines. A second and more mathematically nuanced and perhaps more effective edge-finder is the Canny edge detector[80], which uses a combination of Gaussian filtering, a Sobel operator, and edge tracking with hysteresis to suppress weak edges and emphasize strong ones[81]. Following whichever edge-detection method, the resultant edges are used for circle parameter solving with the Hough transform. Consider any circle in a two-dimensional space. Mathematically, this circle can be described by Equation 1:

[1] $$(x-a)^2 + (y-b)^2 = r^2$$

Where (a,b) is the center of the circle and r is the radius. If the two-dimensional point (x,y) is fixed, the parameters of circle can be found according to Eq. 1. The parametric space is three-dimensional, and all parameters (a,b,r) that satisfy the coordinate (x,y) would lie on a surface of a right-angled cone whose apex is at (x,y,0). In the three-dimensional space, the circle parameters are detected by the intersection of conic surfaces defined by points on the circle.

To find circle parameters if the radius is fixed, the solution space is reduced to two-dimensional, with the coordinates of the circle center being the parameters. For each point (x,y) on the edge of the shape, define a circle centered at that point (x,y) with fixed

radius r according to Eq. 1. The intersection of all of these circles would correspond to the center point of the original circle shape. This idea is summarized by Figure 12, where the four points on the circle on the left are used to generate four circles of fixed radius on the right[82]. The intersection of these circles is the estimated center of the circle on the left.

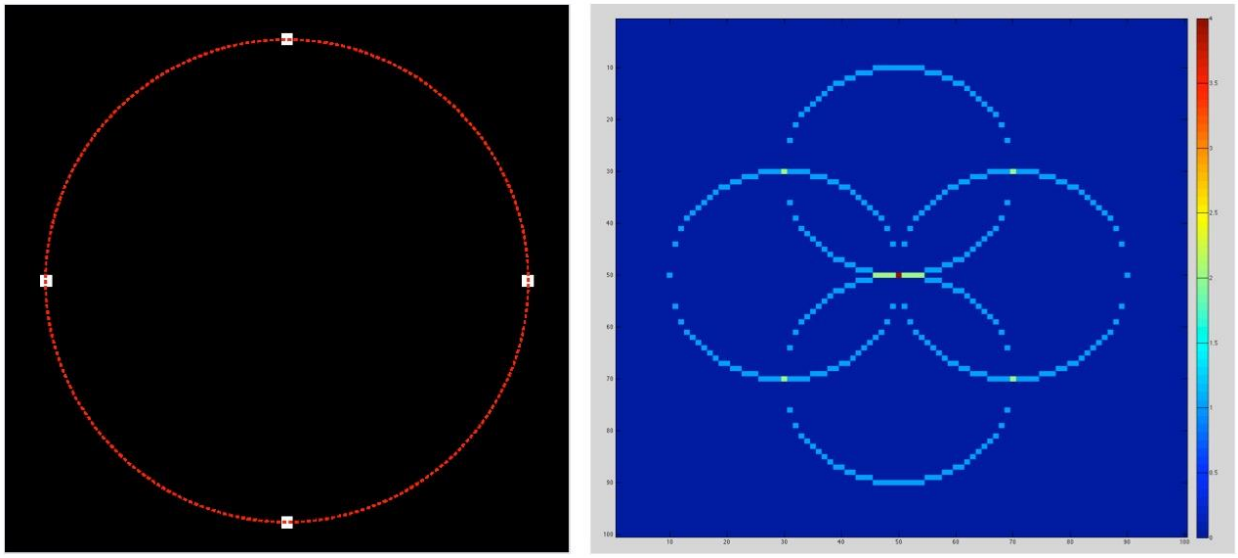

Figure 13: (left) shows a general circle shape. (right) shows four circles generated on four points on the edge of the circle. The intersection of these points is the estimated center of the original circle.

To find circle parameters considering an unknown radius, the parameter space will be three-dimensional. A similar method as shown in Figure 13 can be employed, where we iterate through all radii in the three-dimensional solution space. In this case, the local maxima in the three-dimensional solution space will be the circle center coordinates, with the dimension in the third dimension being the estimated circle radius.

Ellipse detection with the Hough transform is a more difficult problem than circle detection, as the parameter space is five-dimensional[83]; the ellipse's center coordinates, the major and minor axes lengths, and the ellipse orientation. Even still, the process is quite similar to the more simple circle detection case outlined in the previous paragraphs. It is just in a higher-dimensional space that is more difficult to visualize graphically. It is still however just a maximization problem where the overlap of the detected shapes is the solution

containing the five parameters of the detected ellipse, the ellipse center coordinates, major and minor axes lengths. This more complex solution space makes the elliptical Hough transform more sensitive to noise than other forms of the Hough transform, and can lead to increased computational requirements to store the larger multi-dimensional parametric solution space, and compute the optimal ellipse parameters for best shape detection.

2.2.4 – Ellipse Fitting to Breast

The image data in Figure 12 is an example of the input to our implementation of the elliptical Hough transform. In our case, only two ellipse parameters (the major and minor axes lengths) are of interest for our application, which simplifies the problem space and accelerates the computation. We assume the major axis length is the breast separation and the minor axis length is the breast radius. This measurement will be in number of pixels. The pixel spacing is found within the digital imaging and communications in medicine[84] (DICOM) header information of the CT-simulation image data (DICOM tag [0028,0030]), and is used to convert the pixel measurements to centimeters. This work used image data with isotropic voxels of length 1.269 mm. As mentioned in a previous section, we do this breast radius and separation estimation using each slice within the treatment volume. This is identified once again with platinum marker detection. Superficial and inferior markers are placed prior to CT-simulation to denote the

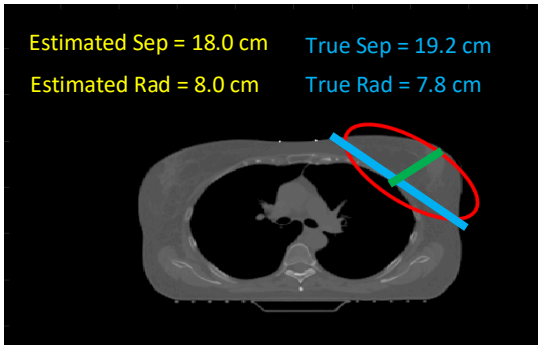

Figure 14: CT-simulation axial slice with fitted ellipse (red) and breast radius (rad) and separation (sep) estimation (yellow) and hand-measurement (blue) of left-breast. Estimated separation and radius from the ellipse major and minor axes length respectively, true separation and radius measured at the blue and green line respectively.

upper and lower bounds of the treatment volume. These markers are identified with intensity thresholding, and are used to begin and end the region in which the breast radius and separation are estimated using the elliptical Hough transform. Figure 14 shows an example Ct-simulation axial slice with the detected ellipse overlaid (red), the estimated left-breast radius and separation measurement from the major and minor axes lengths (yellow), and the actual hand-measured left-breast radius and separation (blue). Included on the figure are the locations where the actual separation and radius measurements were taken in the blue and green lines respectively.

2.2.5 – Comparison with Hand Measurements

The three collected CT-simulation data were used to quantify the accuracy of our automated breast radius and separation framework. For each axial slice within the three treatment volumes, the hand-measured breast separation and radius were compared with the automatically estimated breast separation and radius using the percent difference between the numbers. Additionally, comparing the amount of time the algorithm needs to perform the measurement with the hand-measurements will give an idea as to the clinical applicability of this portion of the framework. Processing that takes too long will not fit in well with the current workflow of breast cancer treatment planning. An accurate estimation of the breast radius and separation in an automated fashion will allow for further modeling of the optimal x-ray fluence. Estimations within a centimeter of the measured breast separation and radius will suffice for this application, as the difference in optimal fluence should not vary too much within a centimeter of the measured breast radius and separation.

2.3 – Results of Automated Radius and Separation Estimation

Within the three treatment volumes, there were 132 axial slices corresponding to 132 breast radius and separation hand measurements and algorithm estimations. Measuring the breast radius and separation by hand took approximately 20 seconds per slice, compared with the automated framework, which took approximately 1.5 seconds per slice including the amount of time to identify the platinum markers which identify the sidedness of the treatment and the span of the treatment volume. That identification is only needed once per volume, so averaged over the entire CT-simulation stack, our proposed algorithm is more time-efficient than hand-measurements. Additionally, there is a certain amount of variability that can be introduced to the planning procedure via hand-measurements. It is reported that procedures such as target volume delineation could have overlaps as low as 10% and standard deviations as high as 60%, which can have substantial dosimetric consequences for the patient over the treatment course[85]. While not assessed in this work, both inter- and intra-reader variability is a relevant problem[86] and is addressed via an automated framework. There is also the fact that our automated algorithm requires much less user input than hand-measurements, freeing up the medical dosimetrist for other important tasks related to treatment planning. Of course, all of this is irrelevant if the automated algorithm is not accurate in its breast radius and separation estimations.

Percent error and error measured in centimeters between the breast radius and separation hand-measurements and the automatic algorithm estimations are found in Table 1. Included are both the individual three collected CT-simulation data averaged over all of the slices in the treatment volume, and the average result across all three. Recall that included in the collected cohort were two left-sided breasts and one right-

sided. Average percent difference between the breast radius measurements over the three test volumes was 12.6% (95% confidence interval 10.4% – 14.8%), corresponding to an absolute measurement error of 0.69 cm (0.59 cm – 0.79 cm). Average percent difference between the breast separation measurements over the three test volumes was 5.2% (95% confidence interval 5.1% – 5.3%), corresponding to an absolute measurement error of 0.92 cm (0.79 cm – 1.05 cm).

Table 1: Agreement between breast radius and separation hand-measurements and automatic algorithm estimations in percent different and centimeter (cm) difference.

Radius		
Number	% Difference	Difference (cm)
1	9.6 [9.3-9.9]	0.70 [0.68-0.72]
2	6.2 [5.7-6.7]	0.40 [0.39-0.41]
3	22.0 [21.5-22.5]	1.00 [0.98-1.02]
Average	12.6 [10.4-14.8]	0.69 [0.59-0.79]
Separation		
Number	% Difference	Difference (cm)
1	6.1 [5.0-7.2]	1.13 [1.11-1.15]
2	4.2 [4.1-4.3]	0.71 [0.68-0.74]
3	5.3 [5.1-5.5]	0.91 [0.71-1.11]
Average	5.2 [5.1-5.3]	0.92 [0.79-1.05]

2.4 – Discussion

2.4.1 – Regions of Overestimation

In slices where the breast had a small radius and separation (radius less than 5 cm, separation less than 14 cm), the automated algorithm tended to overestimate the radius and separation. These slices tended to be towards the superior and inferior portion of the treatment volume. Figure 15 shows and example of this overestimation, where the algorithm estimation disagreed with the hand

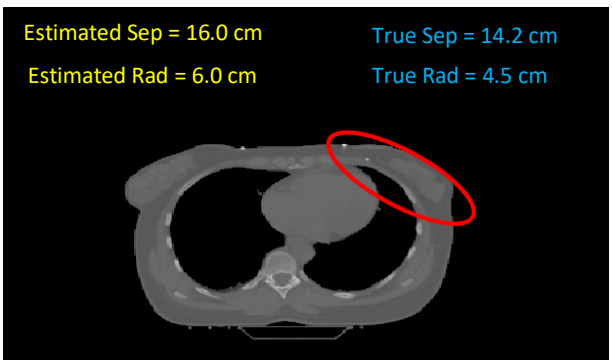

Figure 15: Example of axial slice of a left-sided breast where the automated algorithm overestimated the breast radius (rad) and separation (sep).

measurement with an approximate percent error of 12% for breast separation and 30% for breast radius. This corresponds to a distance error of 1.8 cm for breast separation and 1.5 cm for breast radius. For slices away from the superior and inferior extremes of the treatment volume, the automated algorithm agreed well with the hand-measurements for breast radius and separation, with absolute differences averaging to below 1.0 cm for both radius and separation. If the assessment were to be constrained to regions close to the center of the treatment volume, the percent and absolute difference between the hand-measurements and the proposed algorithm's estimations of the breast radius and separation would be lower.

2.4.2 – Limitations

There are limitations to this portion of the work involved with the use of the elliptical Hough transform for breast radius and separation estimation. We assessed the accuracy using just three collected treatment cases. It is difficult to argue that the entirety of the type of image data that our proposed algorithm might encounter in the clinic is covered within this small test dataset, so outlier examples could potentially give our algorithm difficulty. While our algorithm was essentially unsupervised, there was still the one step of pointing the algorithm to the medial and ipsilateral markers for breast identification and isolation from the rest of the structures in the image data. This is a step that will require an operator at the current state of the project, which hurts the clinical applicability of the algorithm. Even with this supervision, because image-intensity was used to identify the markers, image artifacts might create a condition where the identified medial or ipsilateral marker is actually an artifact region, causing the removal of the wrong portions of the image data via the connecting of the medial and ipsilateral points. This would all but certainly cause

an incorrect breast radius and separation measurement, introducing error into the rest of the optimization algorithm. A limitation specific to the elliptical Hough transform, is that multiple occurrences of the shape can be identified by the algorithm during the same pass. Careful preprocessing was carried out to isolate only the treated breast, but if this were to fail such as in the case of outlier image data, multiple elliptical structures may be identified which could potentially add bias to the breast radius and separation estimation.

2.4.3 – Future Development

This algorithm at its current state takes as input CT-simulation image data, and outputs the breast radius and separation slice by slice. Once the medial and ipsilateral markers are identified, this process is able to be carried out completely unsupervised. Future work will go into fully automating this portion of the algorithm such that the input is the image data and without any operator, the breast radius and separation may be estimated and output. A natural extension of the breast radius and separation that would fully automate this process would be to implement a trained machine learning algorithm to output measurements for the radius and separation using the input CT-simulation slices. Given enough training data and ground truth radius and separation measurements, this could be a relatively easy process to implement using frameworks offered through Keras[87].

Regions of general radius and separation overestimation, such as the inferior and superior portions of the treatment volume when the radius and separation are small, will need special consideration. A gross overestimation of the breast size and shape may cause the modeled x-ray fluence to be suboptimal from a dose homogeneity standpoint, and may even cause the introduction to dose hotspots to these regions. There are other sorts of feature detection algorithms that could be used in this context such as elliptical

template matching[88], Kalman filtering[89], and elliptical local binary patterns[90]. The use of these techniques may improve on the performance of the Hough transform in the superior and inferior portions of the treatment volume. Finally, more examples of CT-simulation data should be put through this framework to have a better idea as to how our algorithm will handle a wider range of image data. This should include some outlier cases such as examples of image data which may be affected with slight image artifacts such as motion or ring.

2.5 – Conclusions

Recall that at the onset of this portion of the project, the starting goal was the development of an automated framework for the estimation of the breast radius and separation using CT-simulation image data acquired prior to the onset of breast cancer treatment. This was important, as the first step of automating the optimization of electronic compensation treatments for breast cancer is estimating the size and shape of the treated breast. To create a model optimizing the x-ray beam fluence to the specific size and shape of the breast, the breast size and shape must be estimated accurately and efficiently for easy implementation to the clinical workflow. For this work, we defined the breast size and shape using the breast radius and separation metric. We considered breast radius to be the measurement from the chest wall to the anterior apex of the breast and breast separation to be the measurement along the posterior edge of the breast. To achieve this estimation, a processing framework was developed in the MATLAB programming environment.

This framework involved the preprocessing of the CT-simulation image data. Platinum markers were placed on the surface of the patient to define the treatment area, in the

cranio-caudal direction, and medial and ipsilateral markers to define the breast volume to be treated. These markers were identified due to their level of x-ray attenuation being many times that of human tissue and the treatment couch, the other two prominent structures in the pre-treatment CT-simulation image data. The medial and ipsilateral markers were used to simplify the image data via the removal of all structure from the image save for the treated breast. The superficial and inferior markers were used to define the starting and stopping points of the treatment volume. The simplified image data was then input to our implementation of the elliptical Hough transform for major and minor ellipse axes length measurement. The major axis length was assumed to be the breast separation, the minor axis length was assumed to be the breast radius. Both of these measurements were carried out in number of pixels. The pixel spacing was extracted from the DICOM file header, and used to convert a number of pixels to a length in centimeters. This breast radius and separation estimation was carried out using each axial slice in the treatment volume as defined by the superficial and inferior platinum markers.

The accuracy of this estimation was assessed via a comparison with hand-measured breast radius and separation in three collected CT-simulation volumes. This comparison was performed using percent difference and absolute difference in centimeters averaged over each of the axial slices in the three volumes. Our results showed good agreement between the hand-measured and proposed algorithm breast radius and separation measurements, averaging to under a 1 cm error between the estimation and actual measurements for both the breast radius and separation over the 3 test volumes. There were some regions of an overestimation towards the breast volume periphery, however general performance was acceptable. Additionally, the computational performance of the

proposed algorithm would fit in well to the current standard clinical workflow, and the proposed method is semi-supervised, where only two clicks from an operator are needed to estimate the breast radius and separation over the entire treatment volume.

With this automated breast radius and separation measurement framework developed, the next step was the development of a mathematical model correlating these breast measurements with the x-ray fluence that can deliver the most homogenous dose distribution throughout the breast treatment volume, and a comparison with other proposed attempts at less-supervised methods for electronic compensation treatment plan optimization.

Chapter 3: Correlating Breast Radius and Separation with Optimal Beam Fluence

3.1 – Summary of Reported Works

3.1.1 – Breast Cancer Treatment with Electronic Compensation

As mentioned in a previous chapter, the introduction of dynamic MLC fingers has allowed for a much more complex delivery of radiation dose such that healthy tissue surrounding the breast treatment volume can be better spared and the breast treatment volume can be more homogenously irradiated with the prescription dose when compared with the use of a standard wedged radiation delivery[91-94]. Electronic compensation using tangentially opposed fields is a technique used for the treatment of breast cancer. This technique is reported to improve the homogeneity of the delivered dose through the treatment volume due to the ability to vary the x-ray fluence across the cranio-caudal direction to compensate for the variation in breast shape and size in the cranio-caudal and anterior-posterior direction[95]. Electronic compensation achieves these improvements in the homogeneity of the delivered dose and the dose savings to surrounding tissue through the motion of the MLC fingers. At certain points during the treatment, the radiation beam can be either partially or fully blocked to modify the fluence of the delivered beam to tissue beneath the fingers. This modulation of beam fluence adjusts the quality of the treatment beam and will change the dose distribution throughout the treatment volume. In regions of the treatment volume where the breast is thinner, the delivered beam can be attenuated such that the thinner portion of the breast is not overdosed. The amount of compensation for missing tissue is defined within the treatment planning software by a metric known as the transmission penetration depth

(TPD). This is the depth along each beamlet path in the x-ray field that the tissue compensation occurs.

3.1.2 – Weaknesses of Forward Planning

In the current clinical practice, the TPD is selected based on the experience of the treatment planner, typically a medical dosimetrist. Dose profiles are computed within the treatment planning software, Eclipse (Varian Medical Systems, California, USA) treatment planning software at our institution, based on the TPD selected by the planner. Electronic compensation is forward planned, so the dose profiles are modified through manual editing of the fluence maps by the medical dosimetrist. This modification is carried out to improve homogeneity within the treatment volume (reduction of radiation hot or cold spots) or to reduce dose delivered to critical surrounding structures. This can be a time-consuming process (upwards of 30 minutes) with large variability between different operators of the treatment planning software based on the operator's skill or experience. It is difficult to ensure that each patient is receiving the best possible treatment plan with such variability introduced to the treatment at the planning stage. It seems likely that a less-supervised technique for TPD selection and x-ray fluence generation may reduce some of this variability, improve the clinical workflow of the medical dosimetrist, and lead to better plans for the patient. It also seems likely that a more patient-specific treatment based on the size and shape (defined by breast radius and separation) of the targeted breast would be a good avenue to explore for improving the treatments.

3.1.3 – Optimizing Treatment to Breast Radius and Separation

Attempts have been published in the literature that have correlated the breast radius and separation to the depth of electronic tissue compensation that yielded the most

homogenous dose distribution. These works have been summarized in a previous chapter, and they all have the same characteristic – they use a single or a few compensation depths over the treatment volume, ignoring the large variation in the breast separation and radius in the cranio-caudal direction.

3.2 – Proposed Algorithm

3.2.1 – Overview of Algorithm

Our work looks to use the breast radius and separation and correlate it to the optimal depth of compensation similar to the previous works. Where we extend on these works is we look to use the breast radius and separation at every axial slice in the treatment volume, and compute the optimal compensation depth at each of these slices. In this way, we believe that plans generated assuming many optimal penetration depths will outperform plans generated assuming either one or a few optimal penetration depths throughout the treatment volume. To this end, a multi-faceted algorithm was developed, the first portion of which was already introduced, which accurately estimates the breast radius and separation at each of the axial slices in the treatment volume in a semi-supervised manner. The second portion is involved with the development of a mathematical model correlating these breast radius and separation measurements to the optimal depth of compensation. It is important to note that this model will be dependent on the selected beam energy of the tangentially opposed field. There will need to be a different model for the 6 MV beam and the 23 MV beam. The third portion is the correlating of these compensation depths (TPDs within Eclipse treatment planning software) to the required x-ray beam fluence needed to deliver the dose to the depths. This last portion is important, as it allows for the bypassing of the treatment planning software to obtain the

x-ray fluence. We can instead input the fluence map for each of the tangentially opposed fields to the treatment planning software, and let the software determine the MLC motion needed to deliver the requested fluence and output the dose distribution curves. In this way, we are taking the fully forward-planned process that electronic compensation typically follows, and moving to a more inverse-planned treatment planning technique[96].

At this point, it is appropriate to define what is meant by x-ray beam fluence. We do not define fluence in the same manner as its physical definition of particles per unit area. Instead, we use the definition of fluence used within many IMRT planning sofware[97], which calls fluence the density of x-rays in the central plane emanating from a point source at a distance 100 cm, normalized to a completely open field[98]. An open beam with static MLC fingers will have a fluence of 1 in the field. Fully blocked, the fluence will be 0. Simply put, the fluence in this work is a unit-less ratio of the x-ray density of the blocked field to the open field, with values between 0 and 1.

3.2.2 – Development of Mathematical Model with Phantom Study

Previous work has developed a mathematical model correlating the breast radius and separation to the optimal TPD[66]. We looked to extend this model all the way to correlating the breast radius and separation to the optimal x-ray fluence needed to achieve the optimal TPD. To do this, semi-elliptical phantoms with uniform intensity were generated using a simple C++ program and input to Eclipse treatment planning software. These phantoms simulated axial slices of the breast with a radius varying from 5 cm to 12

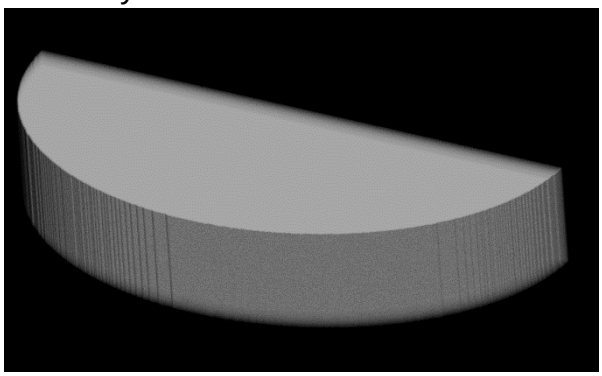

Figure 16: Example volume simulating breast with radius equal to 6 cm and separation equal to 16 cm. In this case, the radius and separation were non-variant in the depth axis.

cm, and a separation varying from 12 to 24 cm, and matched the voxel size (1.269 mm) of the data from our clinical scanner. Initially, these phantoms had uniform radius and separation in the cranio-caudal direction (example volume shown in Figure 16, radius equal to 6 cm, separation equal to 16 cm), but were replaced with phantoms that had a radius and separation which varied in that direction (example volume shown in Figure 17). We felt that this type of phantom better simulated the patient breast and would lead to the development of a more accurate mathematical model correlating the entire breast volume to the optimal beam fluence. It is important to note that in the phantom study, the "phantom" breast radius was equal to half of the generated ellipse minor axis length, and the "phantom" breast separation was equal to the generated ellipse major axis length.

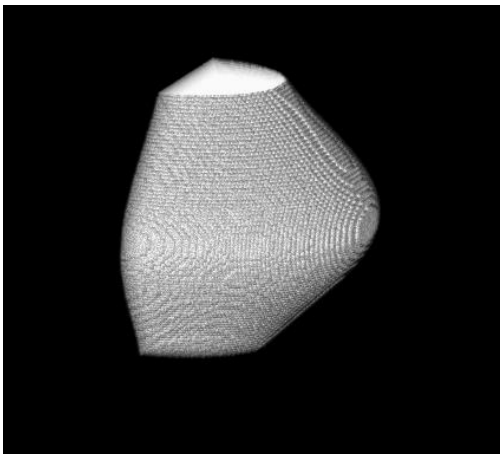

Figure 17: Example volume simulating breast with radius equal to 6 cm and separation equal to 16 cm at the central axial slice. In this case, the radius and separation were changing in the depth axis, better simulating a real breast.

The phantoms with known and varying radius and separation were input to Eclipse, and the TPD was set in-accordance with a previously published model correlating the radius and separation to the optimal TPD[66]. The treatment field size for each of the tangentially opposed fields was set to 20 cm by 20 cm, and the x-ray beam energy was set to either 6 MV, 10 MV, or 23 MV, which are the commonly used energies used in the context of breast cancer treatment with electronic compensation. The x-ray fluence needed to deliver the dose to the compensation depth was measured within Eclipse. This was done for all of the phantoms with the different combinations of radius and separation and for the three beam energies to develop the three models correlating the breast size and shape to the x-ray fluence needed to achieve the compensation depth needed to deliver the optimally homogenous dose distribution throughout the treatment volume. The graphical visualization of the model for the 6 MV beam is shown in Figure 18.

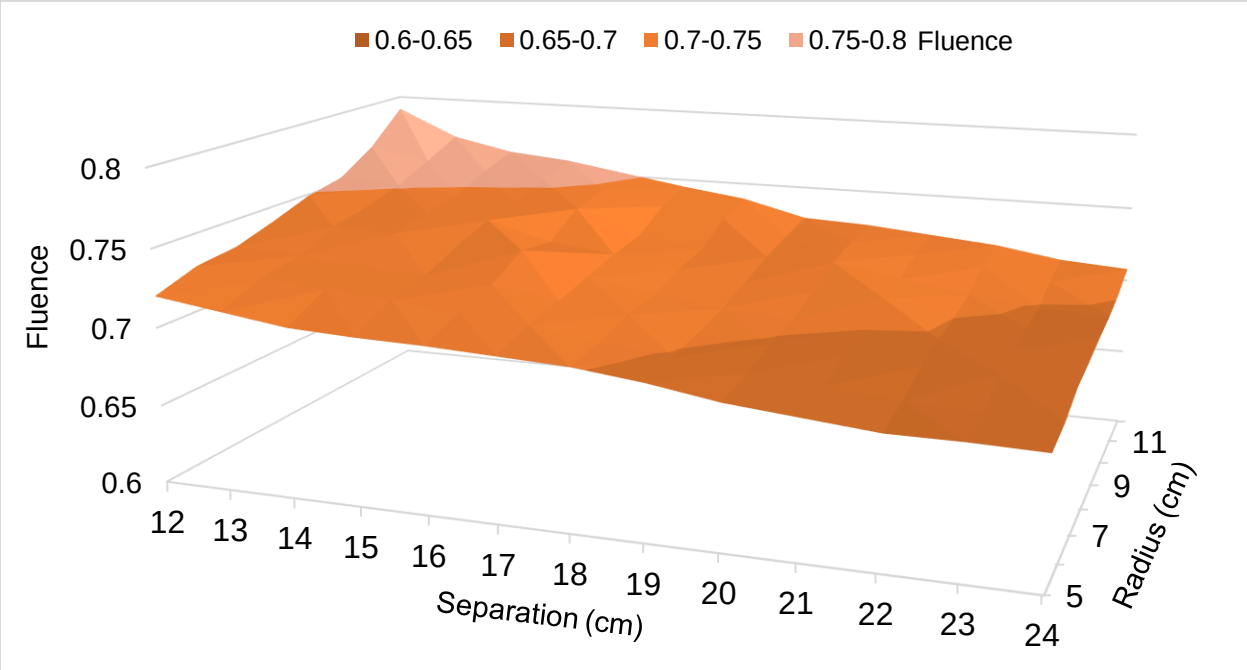

Figure 18: Model correlating the measured breast separation and radius with the x-ray fluence needed to deliver the dose to the compensation depth needed to achieve the most homogeneous delivery throughout the breast volume.

As previously mentioned, there was a different model for each of the three beam energies selected, 6 MV, 10 MV, and 23 MV. To find the mathematical equation which best fits these planes, minimizing the least-square error between the measured model and the proposed equation was carried out. To simplify the number of parameters in the equation and improve the generalizability of the model, we assumed a bilinear fit for each of the three models. The three mathematical fits that were computed are found in Equations 2 through 4,

[2] $$f(radius, separation, 6\ MV) = 0.753 + 0.006 * radius - 0.005 * separation$$

[3] $$f(radius, separation, 10\ MV) = 0.832 + 0.010 * radius - 0.006 * separation$$

[4] $$f(radius, separation, 23\ MV) = 0.888 + 0.006 * radius - 0.007 * separation$$

where radius and separation are the estimated breast radius and separation values output from the work shown in a previous chapter. Each of these fits had good agreement with the measured data (r^2 values of 0.96, 0.94, and 0.92 for the 6, 10, and 23 MV beam fits respectively). These mathematical results are in-agreement with the work of Emmens and James[65] and Alghufaili and colleagues[66], who reported an increase in the TPD needed when the breast separation decreases and the breast radius increases. This portion of the work showed that the TPD is related with the x-ray fluence, in that more fluence is needed to attain a deeper compensation depth, putting our work in-agreement with the literature. These models can be used to compute a mapping of the x-ray fluence delivered to the surface of the breast needed to deliver the most homogenous dose, across all axial slices in the treatment volume.

3.2.3 – Two-Dimensional Fluence Map

It is important to note that these models only correlate the fluence at the surface to the breast to the breast radius and separation. To acquire a comprehensive two-dimensional mapping of the fluence in the beam-eye view, we need to also consider those regions deep from the surface. As each of these beamlets pass into the breast volume, we assume exponential drop-off of the fluence as governed by the Beer-Lambert-Bouguer law[99-101]. This is summarized by Equation 5 and exemplified in Figure 19.

[5] $$Fluence(depth) = Fluence(depth = 0) * e^{-\mu * depth}$$

Where fluence is the intensity of the fluence map at the considered image location some depth from the surface of the breast measured in pixels. μ is the linear attenuation coefficient of the material the beam is transmitting through. In this case, this value was kept a constant value because the phantoms used for this study were uniform in image intensity. In the context of CT, this means that they have a uniform x-ray attenuation throughout the phantom volume. The fluence at the phantom surface was scaled at each pixel location from the

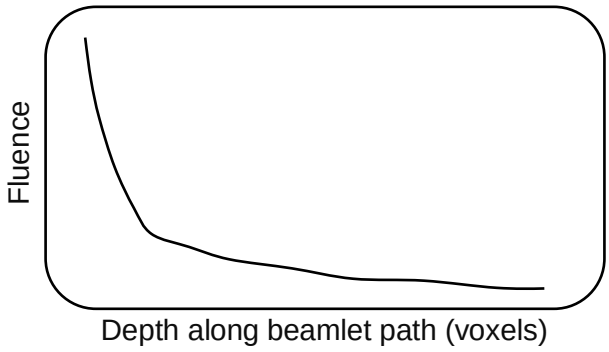

Figure 19: Exemplification of exponential drop-off of beam as it passes through the breast volume. This drop-off follows the Beer-Lambert-Bouguer law.

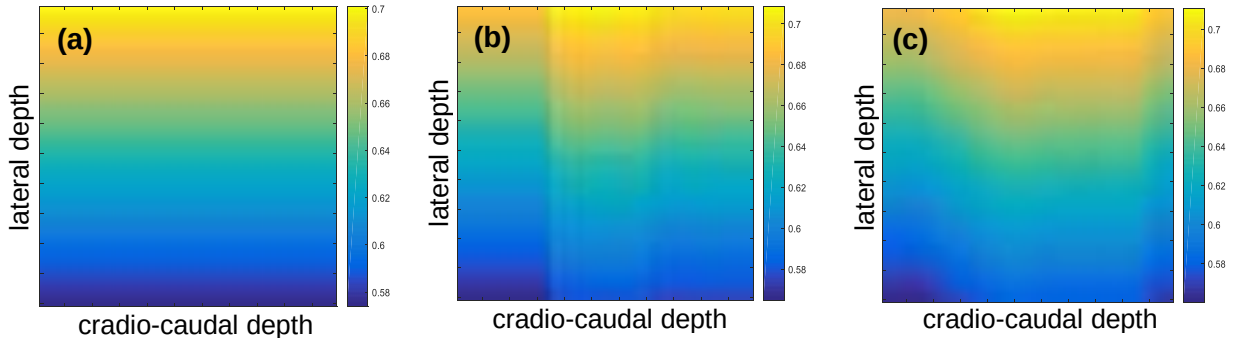

Figure 20: Optimal fluence maps from (a) assuming a single optimal penetration depth, from (b) assuming three optimal penetration depths, and (c) our proposed model which assumes a new penetration depth for each slice in the cranio-caudal direction.

phantom surface to compute the x-ray fluence needed for the most homogenous dose delivery at that point in the treatment volume. In this way, we compute a two-dimensional fluence map that takes into account the variation in breast radius and separation in each axial slice present in the cranio-caudal direction. An example of one of these fluence maps is found in Figure 20, where each fluence measurement is for a different voxel in the CT-simulation data. Included in the figure are the corresponding fluence maps that would have been obtained if a single penetration depth were assumed or if the breast were split into three regions, each with their own optimal penetration depth as previous works published in the literature would have done.

This model correlating the breast radius and separation to the optimal beam fluence at any point in the treatment volume was coupled with the semi-supervised breast radius and separation estimation framework. This created a comprehensive algorithm which takes in as input the pre-treatment CT-simulation image data and outputs fluence maps for each of the tangentially opposed fields for any beam energy that might have been selected due to breast size.

3.2.4 – Comparison in Real Patient Data

To validate this model, actual patient data was needed. Ten electronic compensation breast cancer treatment courses planned and delivered at Roswell Park Comprehensive Cancer Center were retrospectively collected. The pre-treatment CT-simulation image data were anonymized for each patient, and put through our proposed algorithm. Our algorithm estimated the breast radius and separation and used those measurements to obtain two-dimensional x-ray beam fluence maps. These fluence maps were put to Eclipse treatment planning software to generate a new treatment plan. The original

oncologist organ contours were kept, as well as the dose constraints that were placed on the original treatment. The resultant dose distributions from these generated fluence maps were compared with those from the original plans generated by the iterative, manual editing of fluence maps by a medical dosimetrist. Two other plans were generated from each patient course, the first by assuming a single optimal penetration depth determined by taking the average breast radius and separation in the cranio-caudal direction over the entire breast, and correlating it to the optimal TPD using the work published in the literature[66]. This optimal TPD was put to Eclipse, and the fluence maps and resultant dose distributions were generated. This is analogous to the current method, without any dosimetrist optimization. The second plans were generated by recreating the work of Alghufaili and colleagues[66], which we call the three-region breast model. This work broke the breast down to three volumes in the cranio-caudal direction, and using the average radius and separation in each of those regions, three separate TPDs were computed and fluence maps and dose distributions were generated in Eclipse. All four of these plans were quantitatively compared for dose homogeneity using the dose homogeneity index (HI)[102-104], defined in Equation 6.

[6] $$HI = \frac{D_2 - D_{98}}{D_p} * 100\%$$

Where D_2 and D_{98} represent doses to 2% and 98% of the treatment volume respectively, and D_p represents the prescription dose. With this definition of HI given in Equation 6, a lower number is a more homogenous dose delivery to the treatment volume. Pearson correlation coefficients were computed to assess which plans better correlate with the plans of the medical dosimetrist. Institutional dose constraints were additionally used as a comparative metric. Constraints include keeping hot spots at less than 108% the

prescription dose, and cold spots at greater than 95% the prescription dose. Dose to the heart and the volume percent above 20 Gy to the ipsilateral lung were measured due to their status as critical organs near the breast treatment volume. These metrics are important as the heart often receives a biologically significant dose during breast cancer treatments, especially during left-sided breast treatments[105]. This dose puts the patient at risk for conditions such as cardiomyopathy and an increase in heart disease following external beam radiation therapy[106]. It is reported that the ipsilateral lung is at risk for sequelae following breast cancer treatments[107]. Tracking a patient's risk for these conditions is an important part of maintaining the quality of life following treatment. Dose volume histogram (DVH) curves were also output for the breast treatment volume, ipsilateral lung, and heart to compare differences between the techniques[108]. In total, the four planning techniques were compared based on their ability to meet the institutional dose constraints, homogenously deliver dose to the treatment volume, and reduce dose delivered to the heart and ipsilateral lung. The amount of time it took our proposed algorithm to generate each plan was also measured. This included the breast radius and separation estimation portion of the algorithm, as well as the mathematical model correlating the radius and separation to the required x-ray fluence.

3.3 – Results of Treatment Plan Comparison

Our proposed algorithm generated plans in around 20 seconds averaged over all ten of the treatment courses. This compares well with the medical dosimetrist plans, which can take up to 30 minutes due to the iterative and manual process of editing the fluence maps to bring the generated plans within institutional dose constraints. It is also important to

note that our proposed algorithm requires much less user input than the classical forward planned iterative method. This is an improvement to the clinical workflow.

Table 2: Summary of dose homogeneity indices (HI) for all ten collected treatment courses. Included in this comparison are the treatments generated with our proposed algorithm, plans created using the three-region breast model, those plans manually optimized by a medical dosimetrist, and plans generated by assuming a single compensation depth (TPD) throughout the entire treatment volume. There was no statistical difference between HI measured from our proposed algorithm's plans and the medical dosimetrist' plans as assessed with a Student's T-Test.

Number	Proposed Work HI	3-region breast model	Dosimetrist Optimized HI	Single TPD HI
1	26.7	22.4	16.5	23.0
2	17.8	19.2	14.1	19.1
3	10.6	15.2	11.2	17.2
4	11.8	14.6	9.51	13.3
5	8.49	7.87	3.32	8.04
6	8.79	14.1	6.64	12.6
7	4.59	7.44	3.82	8.19
8	7.57	21.5	8.84	23.5
9	11.3	17.9	8.29	18.7
10	10.6	16.0	10.5	17.8
Average	12.6	15.6	9.87	17.0

Table 2 summarizes the dose HI for each of the ten collected electronic compensation treatment courses comparing the original plans created by the iterative process of the medical dosimetrist, our proposed semi-supervised algorithm, those plans generated assuming the three-region breast model, and the use of a single optimal penetration depth over the breast treatment volume. The HI for plans generated using our proposed algorithm averaged to 12.6 over the ten collected courses. This is in comparison with plans from the medical dosimetrist, whose average HI over the ten courses was 9.87. This difference between the two techniques was not significant, as assessed through a two-tailed heteroscedastic Student's T-Test[109]. This is a positive result, as statistically our algorithm generates plans that are non-inferior to the plans generated by the medical dosimetrist. These plans are created with much less user supervision and in much less

time. The other two techniques both had HI averages that were higher than that of our proposed algorithm, 15.6 for the three-region breast model, and 17.0 for the single TPD technique. All but the single TPD plans had their minimum HI value from the same treatment course, 4.59 for our proposed algorithm's plan, 3.82 for the medical dosimetrist plan, and 7.44 for the three-region breast model's plan. This was the similar for the technique's maximum HI; it came from the same collected course. The HI from this course was 26.7 for our proposed algorithm's plan, 16.5 for the medical dosimetrist plan, and 22.4 for the three-region breast model. Our proposed algorithm created plans that bettered the medical dosimetrist plans in terms of dose homogeneity in two of the ten courses, bettered the plans from the three-region breast model in eight of the ten courses, and bettered the plans from using a single TPD in nine of the ten courses. Additionally, Pearson correlation coefficients indicated that our algorithm's plans' HI better correlated with the dosimetrist plans HI (0.868) compared with both the three-region breast model's plans' HI (0.827) and the single TPD model's plans' HI (0.797). This indicates that our algorithm is able to generate treatment plans that better correlate with the clinical standard expert plans.

Table 3: Summary of global dose maximum and treatment volume (CTV) minimum dose values for all ten collected treatment courses. Included in this comparison are the treatments generated with our proposed algorithm, plans generated using the three-region breast model, those plans manually optimized by a medical dosimetrist, and plans generated by assuming a single compensation depth (TPD) throughout the entire treatment volume. Our proposed algorithm generated plans that satisfied institutional dose constraints (global dose maximum less than 108% prescription dose, CTV dose minimum greater than 95% prescription dose) at an equal rate to the medical dosimetrist plans.

	Global dose max (% Prescription)				CTV dose min (% Prescription)			
Number	Proposed Work	3-region breast model	Dosimetrist Optimized	Single TPD	Proposed Work	3-region breast model	Dosimetrist Optimized	Single TPD
1	107.7	108.5	109.1	113.3	96.9	97.3	104.1	96.0
2	109.7	111.3	106.5	111.8	74.4	75.0	76.9	74.2
3	107.4	108.1	107.5	112.7	95.5	88.7	95.3	89.1
4	107.5	110.4	105.9	109.8	95.5	95.2	95.0	96.8
5	107.7	109.7	104.0	105.0	95.1	95.9	98.1	87.8
6	107.5	108.7	105.5	111.4	97.9	96.0	99.3	97.4
7	108.0	114.2	105.9	116.3	95.4	95.4	95.7	95.4
8	107.6	112.6	106.6	114.6	95.3	92.8	97.8	94.1
9	107.5	115.5	106.0	118.1	95.6	95.6	95.1	95.0
10	107.5	108.6	107.8	114.4	86.1	81.6	87.8	87.2
Average	107.8	111.2	106.5	112.7	92.7	91.4	94.5	91.3

Table 3 summarizes the global dose maximum and treatment volume dose minimum for each of the ten collected courses. Recall that an institutional dose constraint was that the global dose maximum must remain below 108% the prescription dose and the treatment volume dose minimum must remain above 95% the prescription dose. Our algorithm's plans matched the dosimetrist plans in satisfying the maximum dose constraint (less than 108% prescription dose) in nine out of ten of the collected courses, and the minimum dose constraint (greater than 95% prescription dose) in eight out of ten cases. The specific courses where the plans fell outside of constraints were in cases of large breasts where delivering a homogenous dose throughout the treatment volume is the most challenging. In cases like these, the treatment was still delivered using the dosimetrist plans, even though it lied out of dose constraint. Both the three-region breast model and the use of a single TPD generated plans which did not meet the maximum dose constraint in a single collected course. The three-region breast model generated plans which met

the minimum dose constraint in eight out of ten courses, while the single TPD technique met the minimum dose constraint in five out of the ten collected treatment courses. Clearly, our proposed algorithm was better able to meet our institutional dose constraints compared with the three-region breast model and the use of a single TPD throughout the treatment volume. Once again, our proposed algorithm was non-inferior to the medical dosimetrist plans.

Table 4 summarizes the mean dose to the heart contour and the volume percent above 20 Gy to the ipsilateral lung ($V_{20\ Gy}$) over the ten collected courses. Our proposed algorithm's plans $V_{20\ Gy}$ averaged over the ten collected courses was 149 cGy compared with the 104 cGy the medical dosimetrist plans delivered to the heart. The discrepancy between the two numbers can be explained by a single case (number 10), a left-sided breast treatment, where manual blocking of the field over the heart was performed in the dosimetrist plans to reduce the mean heart dose. This blocking was not done in any of the semi-supervised techniques, so the mean heart dose is higher in the plans from the other three techniques for this course. Considering the ipsilateral lung $V_{20\ Gy}$, the percentages are similar across the four techniques. All are well within the institutional tolerances. Ignoring this case (number 10) where there was some manual blocking of the field, in terms of mean dose delivered to the heart and the ipsilateral lung $V_{20\ Gy}$, there was no statistical difference indicating between our algorithm's plan and the medical dosimetrist plan.

Table 4: Summary of mean dose to the heart and the ipsilateral lung $V_{20\ Gy}$ for all ten collected treatment courses. Included in this comparison are the treatments generated with our proposed algorithm, plans generated using the three-region breast model, those plans manually optimized by a medical dosimetrist, and plans generated by assuming a single compensation depth (TPD) throughout the entire treatment volume. Ipsilateral lung $V_{20\ Gy}$ is similar for all four techniques. Mean dose to the heart is similar between the four techniques save for course number 10. This specific case had manual blocking of the x-ray field in the medical dosimetrist plan which reduced the heart dose. The other three techniques did not have this blocking and had correspondingly larger mean heart doses delivered by the treatment.

	Mean dose to the heart (cGy)				Ipsilateral lung $V_{20\ Gy}$ (%)			
Number	Proposed Work	3-region breast model	Dosimetrist Optimized	Single TPD	Proposed Work	3-region breast model	Dosimetrist Optimized	Single TPD
1	11.0	15.0	13.7	13.4	0.42	2.30	2.41	2.05
2	298	296	294	327	18.2	18.3	16.7	20.3
3	177	165	109	160	5.12	4.91	3.56	4.65
4	271	267	149	250	9.09	9.03	8.07	7.93
5	40.8	44.9	39.7	42.0	16.6	16.8	15.8	16.2
6	113	112	108	111	8.95	8.84	8.33	8.59
7	47.0	52.4	47.7	51.7	9.56	11.2	9.9	10.9
8	26.9	28.9	26.5	28.7	11.4	11.2	11.4	10.9
9	95.9	128	89.5	125	9.18	10.8	7.8	10.6
10	406	402	159	397	18.7	18.5	12.4	18.2
Average	149	151	104	151	10.7	11.2	9.65	11.0

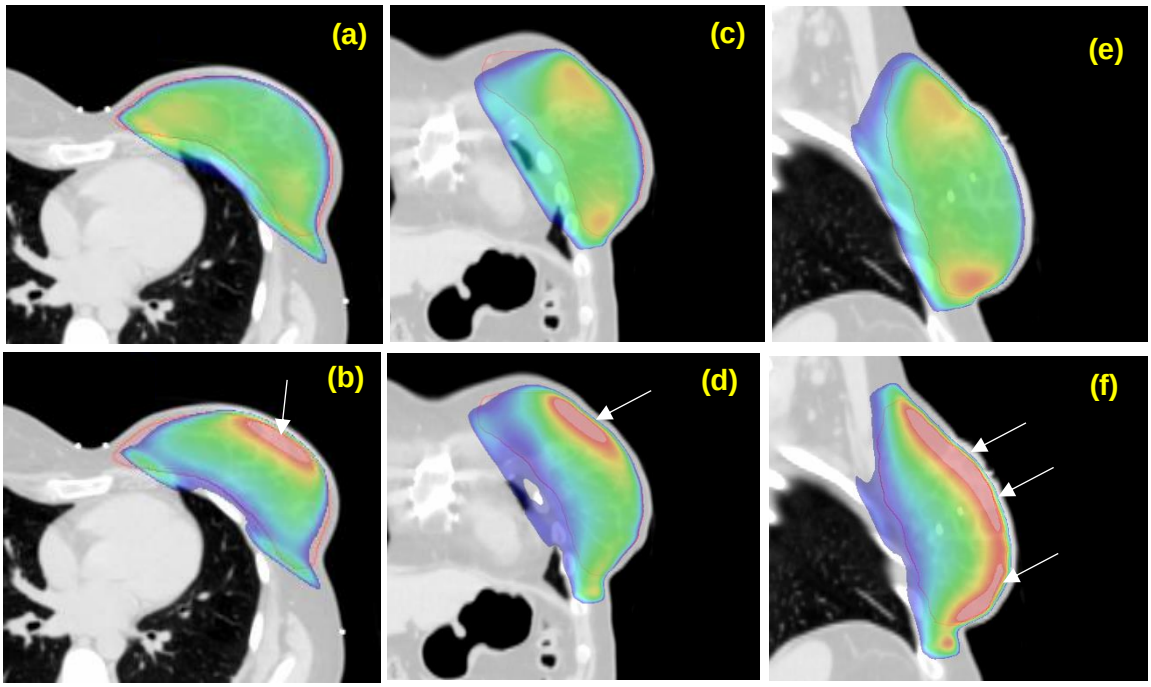

Figure 21: (a,c,e) axial, coronal, and sagittal views of the breast treatment volume showing the isodose color washes from the treatment plan generated with the proposed algorithm. This plan's measured homogeneity index was 10.6. (b,d,f) axial, coronal, and sagittal views of the breast treatment volume showing the isodose color washes from the treatment plan generated by assuming a constant transmission penetration depth of 30%. This plan's measured homogeneity index was 17.2. Note the anterior hotspot present in the isodose color washes in the single penetration depth plans (white arrows). This hot spot is not present in our algorithm's plans.

Figure 21 demonstrates isodose color washes in the axial, sagittal, and coronal planes. One set were generated from fluence maps computed within our proposed algorithm, the other from the current method utilized in the Eclipse TPS that assumed a constant TPD over the entire treatment volume. Qualitatively, our proposed algorithm creates a plan that has a more homogenous dose coverage throughout the breast, and a reduced anterior hotspot, indicated with the white arrows. This specific case (number 3 in Tables 2-4) had a HI of 10.6 from our algorithm's plan and an HI of 17.2 from the plan assuming a single TPD of 30% throughout the breast volume. Assuming the three-region breast model generates a treatment plan that yielded an HI of 15.2 for this specific course. The medical dosimetrist optimized plan yielded an HI equal to 11.2 for this treatment course. Figures 22 through 24 show dose volume histograms from the breast treatment volume (Figure 22), ipsilateral lung (Figure 23), and the heart (Figure 24) comparing the treatments generated using our proposed algorithm (triangle points in DVH curves) and the original medical dosimetrist treatment (square points in DVH curves). These DVH curves were measured from course number 8 in Tables 2-4, and show that for this case,

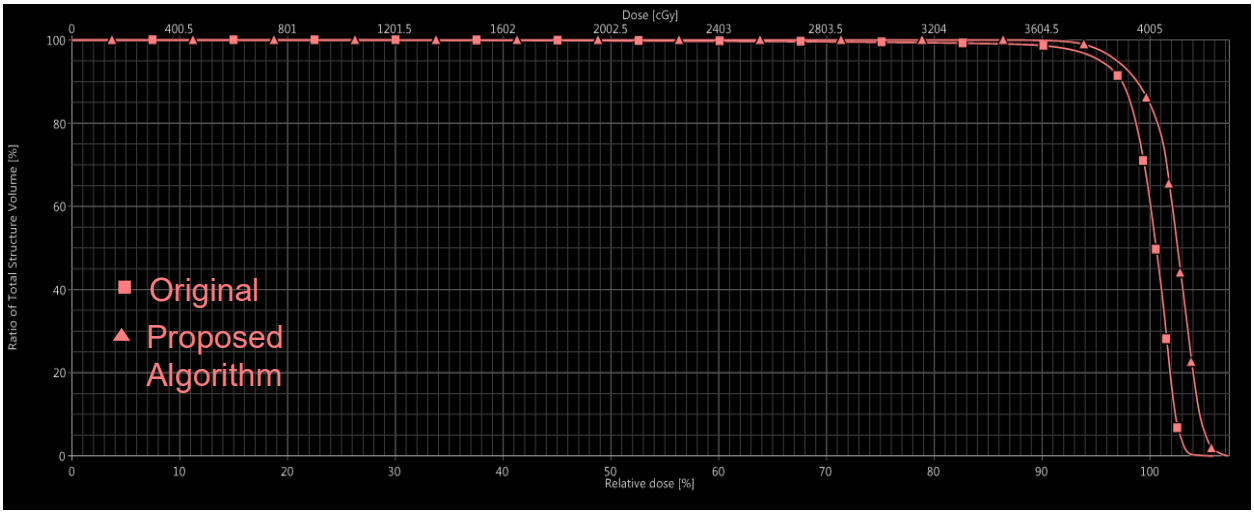

Figure 22: Dose volume histogram curves throughout entire breast treatment volume for our proposed algorithm's plan (triangle) and the original medical dosimetrist plan (square). This specific case yielded homogeneity indices of 7.57 for our algorithm's plan and 8.84 for the original plan indicating a more homogenous delivery of dose throughout the treatment volume using our algorithm's plan.

there is better homogeneity throughout the treatment volume (DVH curve better approaches prescription dose of 40.05 Gy) and similar ipsilateral lung and heart doses. All ten of the courses do not necessarily pose as compelling of an argument, but statistically non-inferior performance coupled with an improvement in the clinical workflow indicate some clinical value to this sort of processing and treatment planning.

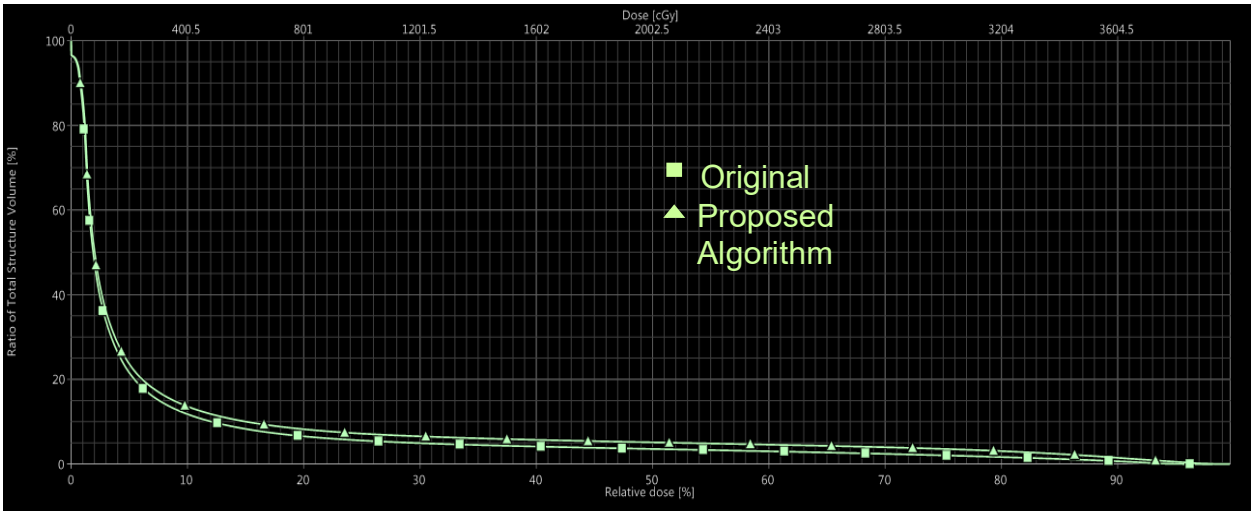

Figure 23: Dose volume histogram curves for the ipsilateral lung for our proposed algorithm's plan (triangle) and the original medical dosimetrist plan (square). This specific case yielded ipsilateral lung $V_{20\ Gy}$ of 11.4% for both of the two treatment techniques.

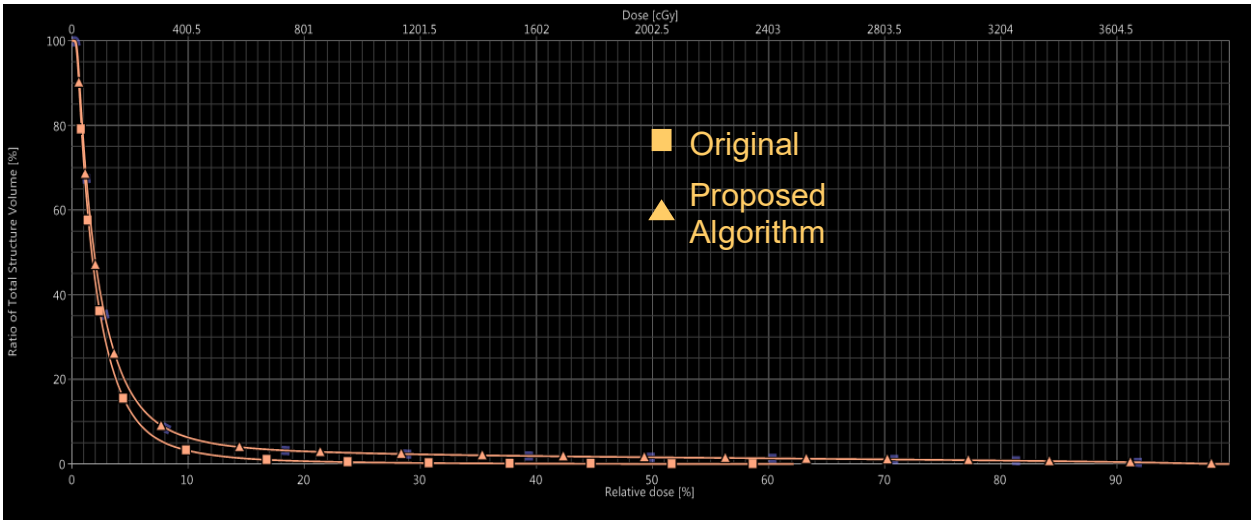

Figure 24: Dose volume histogram curves for the heart from our proposed algorithm's plan (triangle) and the original medical dosimetrist plan (square). This cases yielded a mean heart dose equal to 26.9 cGy compared with a mean heart dose of 26.5 cGy for our proposed algorithm' plan and the medical dosimetrist plan respectively.

3.4 – Discussion

3.4.1 – Isodose Color Wash Comparison

A comparison of the isodose color washes in Figure 21 shows better coverage of the green color wash area over more of the treatment volume in the three views when the plan from our proposed algorithm is used instead of the single TPD of 30%. In the axial slice (Fig. 21a and 21b), the green wash extends closer to the posterior edge of the breast volume up to the lung volume. The sagittal view (Fig. 21e and 21f) shows an advantage with using our proposed algorithm in terms of the coverage of the green wash towards the inferior portion of the breast volume. In all three of the views, the green wash is more homogenously delivered throughout the treatment volume, as confirmed with the HI measurement for this case (10.6 for the proposed algorithm plan, 17.2 for the single TPD plan). In the proposed algorithm plan there is a noted reduction in an anterior radiation hot spot that is prevalent in all three of the views from the single TPD plan. This can be clinically significant, as it are these hot spots which can cause the radiation therapy adverse effects often reported in the literature. This reduction in the hot spot can be attributed to using the information present in the entire treatment volume (breast radius and separation) to generate the treatment plan, as opposed to just a single axial slice.

3.4.2 – Mathematical Models

When considering the mathematical models fitted for the 6 MV, 10 MV, and 23 MV treatment beams (Equations 2, 3, and 4 respectively), they are all dominated by the DC additive component. The breast radius and separation both play a roll; additive for the radius, subtractive for the separation, but this roll is small numerically. Even with this small numerical tuning of the models with the breast radius and separation, there is a large

difference in how the dose is delivered through the treatment volume. A small change in the beam fluence delivered over the course of many fractions can have a large impact by the end of the treatment, as confirmed by Tables 2-4, the isodose color washes in Figure 21, and the DVH curves in Figures 22-24.

3.4.3 – Regions of Overdosing

As discussed in a previous chapter, with breasts of small separation and radius, our semi-supervised size estimation algorithm tends to overestimate the radius and separation. This is also true in the extreme superior and inferior regions of the treatment volume, where the breast radius and separation tend to be small, less than 5 cm and 14 cm for the radius and separation respectively. An overestimation of the breast radius and volume would be input to our mathematical model, and result in a beam fluence that is higher than what would actually be optimal for that specific axial slice. This could result in regions of overdosing depending on the accuracy of the radius and separation estimation, causing radiation hot spots and reducing the homogeneity of the treatment plans. Of the collected courses where there was a large disparity between the dosimetrist plans and our proposed algorithm's plans, there were regions of overestimation by our semi-supervised radius and separation algorithm. This led to a reduction in the HI. It makes sense that in these cases, some manual fluence optimization would be necessary to reduce these hotspots present in the dose profile.

3.4.4 – Our Algorithm in the Clinical Workflow

We think of this work as a potentially more homogenous starting point for the iterative forward planning process of the medical dosimetrist. Currently, a single TPD is empirically selected within Eclipse treatment planning software, and the resultant fluence maps are

manually edited to improve the homogeneity of the calculated dose profiles and bring the treatment plan to within the institutional dose constraints. Our work has shown that our semi-supervised algorithm that estimates the breast radius and separation over the entire treatment volume using elliptical fitting via the Hough transform and relates them to the x-ray fluence required to deliver the most homogenous treatment plan can improve on the use of a single compensation depth in terms of satisfying dose constraints and homogeneity of the treatment plan. When our algorithm's plans are compared with the dosimetrist plans, there is statistically nothing between them in terms of dose homogeneity, however numerically there is a difference. Considering mean dose to the heart, the dosimetrist's ability to add additional x-ray field blocking to protect the heart leads to a reduction in the mean heart dose. This type of blocking is currently not possible with an algorithm like this, so there will still be a role for the medical dosimetrist in the planning room. Starting from a plan generated with our proposed algorithm instead of one assuming a single compensation depth throughout the treatment volume should lead to a quicker manual editing of the fluence map to bring it within institutional dose constraints and optimize it for dose homogeneity. In each of the ten collected cases, there was some combination of the global dose maximum being too high (greater than 108% of the prescription dose) or the treatment volume minimum dose being too low (less than 95% of the prescription dose) from the single TPD plans, which would necessitate manual fluence map editing by the dosimetrist. In the cases where these dose constraints were met by the original medical dosimetrist plans, our algorithm was able to create plans which satisfied the same constraints in a semi-supervised manner. There may be some manual editing required to achieve equivalent dose homogeneity, ipsilateral lung $V_{20\,Gy}$, or mean

dose to the heart, however compared with the use of a single compensation depth or even three as used in the three-region breast model, the plans from our algorithm attain a higher level of homogeneity and are more deliverable considering institutional dose constraints.

Figure 25 is an exemplified flowchart as to how our algorithm would fit into the current clinical workflow. The patient' CT-simulation data is acquired and put to the proposed algorithm which couples a breast radius and separation estimation framework with a mathematical model to correlate the measurements to the required optimal fluence. This outputs a two-dimensional fluence map that is readable by Eclipse. Once this map is put into Eclipse, the MLC motion and the dose profiles of the planned treatment are computed. It is at this stage that any required manual editing of the fluence map by the medical dosimetrist can be carried out. This editing may be done to further protect the heart or the lung volume, or may be necessary due to a patient with a small breast size where the radius and separation might have been overestimated. However, this editing should require fewer iterations when compared with starting from a plan that assumed a

single compensation depth. This flowchart can be compared with the one from Figure 6, which shows the current clinical standard method for the forward-planning procedure.

3.4.5 – Project Limitations

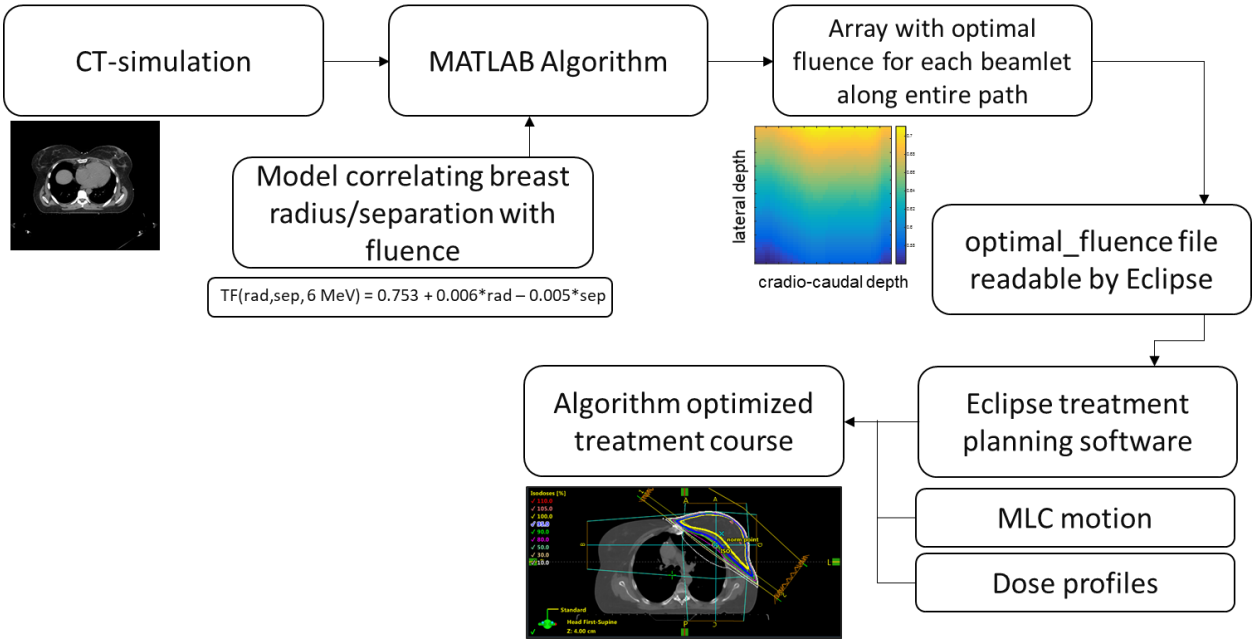

Figure 25: Flowchart showing proposed algorithm's implementation to clinical workflow. Our algorithm uses image data that is already clinically acquired in the current workflow, and can obtain a treatment course with it in a semi-supervised manner. Following the output of the plan, a dosimetrist can manually edit the fluence maps as necessary. Compared with the current clinical method, the proposed algorithm's plan should require less editing than the current standard method of assuming a single compensation depth.

A limitation of this current work is it was developed using breast phantoms of uniform image intensity. This means that the x-ray attenuation of the phantoms is uniform as well. For our assumption of exponential drop-off of the fluence from the surface of the breast into the treatment volume as governed by the Beer-Lambert-Bouguer law, this is required. It is not the case in a real breast volume. It is this fact that may have caused the estimated optimal two-dimensional fluence map to be actually optimal in the actual patient from a homogeneity standpoint.

An additional limitation is in clinical cases where there is skin folding at the breast surface, either at the point of CT-simulation or during treatment. The breast radius and separation

might not be impacted, but the optimal depth of compensation would be changed, which would not be accounted for in our model. This would lead to the generation of suboptimal plans that would need some manual editing by a dosimetrist prior to treatment delivery.

A third limitation of this study is the relatively small number of collected courses that were analyzed with our algorithm. Ten treatment courses is probably not enough to get a good sampling of the breadth of cases that may be encountered in a typical clinical setting. It is unknown at this time how outlier cases would be handled by our algorithm. If there are image artifacts present in the initial CT-simulation, the estimation of the breast radius and separation may be negatively affected which could throw the entire treatment plan generation off. This could include the attenuation information used for dose computation, so if the artifacts were bad enough as can happen with motion artifacts, the image data would be reacquired.

A fourth limitation of this work is how the plans were assessed solely with metrics that pertain to the quality of the treatment plan. The question persists if the differences in homogeneity index between our proposed algorithm's plans and the plans from the medical dosimetrist are clinically relevant. Statistically we know them not to be, but would the patient be clinically impacted one way or the other due to differences in the treatment. The patient outcome is the focus of all treatments and research in the context of radiation therapy, and the metrics selected for this work cannot directly show any differences one way or the other in terms of the clinical outcome.

Lastly, we assumed a bilateral fitting for the mathematical model correlating the breast radius and separation to the beam fluence needed to deliver the optimal dose distribution throughout the treatment volume. This was done to ensure that the computational

efficiency of the model could be as high as possible, without using too coarse of a fit to the measured results. We also did not want to overfit to the data the model was obtain using. It was only ten cases, hence it is possible that it does not represent the actual width of cases seen clinically. It is possible that a more mathematically nuanced model could better represent the measured data, without missing the generalizability or the computational efficiency of a bilateral fit. Some of the regions of inhomogeneity could have been introduced due to assuming too simplistic of a model.

3.4.6 – Future Directions

A natural extension of this work is to implement some sort of machine learning approach to the algorithm, whether it be just the breast radius and separation portion of the work, or the output of the two-dimensional fluence map. It seems likely that the addition of some artificial intelligence capabilities would assist in the treatment planning for electronic compensation breast cancer treatments, or even radiation therapy in general. A data-driven strategy which can use patient-specific information such as demographics in ensemble with the pre-treatment CT-simulation image data should help with the decision making that goes on during the treatment planning stage. This might also add the capability of patient-specific blocking of the x-ray field, if it is predicted to deliver too much dose to the heart or other critical structures near the treatment volume. In fact, there is already work being published regarding machine learning and artificial intelligence as a viable technique in the context of radiation therapy treatment planning and the radiation oncology practice as a whole[110-112].

More treatment courses should be collected and assessed with this proposed algorithm. This would give a better idea as to how the algorithm might handle outlier examples and

would allow for tuning of the mathematical model if it is seen that there is a general error in certain regions of the breast volume or in breast sizes of a certain radius and separation.

Using a more mathematically nuanced fit with more parameters may improve the results. Other fitting equations correlating the breast radius and separation with the optimal fluence should be investigated for computational efficiency, generalizability to the entire dataset, and actual dose metrics to see if gains can be realized with a different fit.

Finally, if this algorithm were to ever be considered for actual clinical implementation, a prospective study would have to be carried out which compared the current clinical standard of a single compensation depth with dosimetrist editing against our proposed algorithm with dosimetrist testing. Two cohorts would be collected, each being treated with one of the techniques. Such a comparison would use similar metrics as used in this work, but could also include clinical outcomes controlled for patient demographics. Dosimetrist opinion could be collected as well. Does our proposed algorithm actually improve their clinical workflow? Is our algorithm still too supervised to be that much of an improvement over the current standard? Such a study would be powerful, in that the patient outcome could be assessed and analyzed along with the dose metrics and the other comparisons.

3.5 – Conclusions

Recall that at the outset of this portion of the work, the goal was to develop a mathematical model correlating the breast radius and separation with the required x-ray beam fluence needed to deliver a treatment with optimal dose homogeneity. This was done by generating uniform semi-elliptical phantoms with varying radius (ellipse minor axis length

divided by 2) and separation (ellipse major axis length). These phantoms simulated breasts seen clinically. The optimal compensation depth at each of the axial slices in the treatment volume was set based on published work, and the fluence needed to deliver a dose with the set compensation depth was measured within Eclipse treatment planning software. With these measurements, we carried out a least-square error minimization problem, assuming a bilateral fit to come up with models correlating the breast radius and separation with the required fluence. These models do depend on the beam energy of the specific field. These models were coupled with the semi-supervised breast radius and separation framework from an earlier chapter, and assessed using ten collected electronic compensation treatment courses. CT-simulation data is input to the model, and a two-dimensional fluence map is output that is used by Eclipse to generate the dose distributions. The treatment plans generated via our proposed algorithm were compared against the original dosimetrist optimized plans, as well as two other planning techniques – using a single compensation depth throughout the treatment volume and no editing of the fluence maps, and breaking the breast up into three regions and using three compensation depths in each of the regions. This was done to assess if any gains could be found by considering the full volumetric shape of the breast. There is large variation in the cranio-caudal direction in-terms of the breast radius and separation, hence it was believed that the proposed algorithm's plans would out-perform those plans from a single or three compensation depths, and would hopefully approach the performance of the plans generated from the iterative and manual editing of the fluence maps by the medical dosimetrist. This would be in-terms of the dose homogeneity index, institutional dose constraints

Our results indicated that this was the case. There was an improvement in the homogeneity of the delivered dose in plans from our algorithm when compared with the plans from assuming a single or three compensation depths. Our algorithm's plans were more deliverable compared with using a single or three compensation depths considering institutional dose constraints of global dose maximum and treatment volume dose minimum. It seems likely, based on these results, that there is some value gained by considering the entire breast volume instead of just one or a few measurements throughout the breast.

Comparing our algorithm's plans with those optimized by the medical dosimetrist, they were statistically identical using the homogeneity index metric, mean dose to the heart (if we ignore the case where there was manual blocking of the field), ipsilateral lung $V_{20\ Gy}$, and the institutional dose constraints. Where our algorithm might improve on the current clinical standard is in the amount of manual supervision and time needed to attain these treatment plans. Our algorithm is able to generate a plan from the CT-simulation data in around 20 seconds. This compares favorably with the manual and iterative current process, which can take up to 30 minutes.

We envision processing such as this being clinically useful as a more homogenous starting point for the manual and iterative process of electronic compensation radiation therapy treatment planning. The medical dosimetrist may be able to more quickly edit plans, to satisfy the institutional dose constraints, from our algorithm compared with those generated assuming a single constant compensation depth, which is how it is currently done. This may lead to improvements in the clinical workflow, would reduce some of the variability introduced into the treatment planning process through the manual and iterative

forward-planning process that is currently the clinical standard, and may improve the clinical outcomes of the patients undergoing electronically compensated radiation therapy for breast cancer.

Chapter 4: Future Directions and Project Conclusions

4.1 – Future Directions

There is still much work to do to prove the actual clinical utility of the algorithm proposed in this thesis. More treatment courses are needed, both to further develop the algorithm used to estimate the breast radius and separation from the axial CT-simulation image data, as well as to better tune the mathematical models used to correlate the breast radius and separation with the optimal x-ray beam fluence. The ten collected treatment cohorts in the initial cohort were finely curated for this task. The breast sizes were all within the typical clinically seen range (radius between 5 cm and 12 cm, separation between 12 cm and 24 cm), and there were minimal artifacts present in the image data. All of the image data were acquired on the same model of CT scanner, and they were all from the same institute. It is unknown how successful our proposed algorithm would be using a dataset collected from multiple institutions, potentially from multiple different types of CT scanners. The different acquisition parameters such as slice thickness, reconstruction algorithms, and dose levels might require some tuning of the algorithm, especially on the side of the breast radius and separation estimation. Additionally, other institutions may employ slightly different institutional dose constraints that may necessitate different amounts of two-dimensional fluence map editing by the medical dosimetrist to bring the generated plans to within tolerance. A more expansive collection of image data and treatment courses would allow assessment of the generalizability of the model, much better than the original ten collected courses from our institution allowed for.

As stated in an earlier chapter, our algorithm is not completely automated. The estimation of breast radius and separation portion of the algorithm requires the identification of two platinum markers by an operator (exemplified in Figure 10), a medial and an ipsilateral marker. It is a small bit of supervision required, but the clinical workflow would be greatly improved if the full algorithm were completely automated. Full automation would allow the two-dimensional fluence maps to be generated right at the point of CT-simulation. The medical dosimetrist could then review the maps and make whatever modifications were needed to bring the dose distributions to within the institutional dose constraints. There are several ideas[113-115] as to how to fully automate this step, some more complex than others, and should be the focus of future work. Some ideas will be summarized here. An atlas-based identification of the markers could be a good avenue to begin. The markers generally are placed in the same region on the patient, as they help define the in-plane treatment area. This basis knowledge could be utilized in the preprocessing scheme to automatically identify the markers, or at least automatically point the intensity thresholding to the regions of the markers. A second avenue could be the implementation of machine learning to the problem. This could be done at many different levels, with different data requirements for each. The task of marker identification could be put to a machine learning algorithm. The entire estimation of breast radius and separation could be automated using machine learning. Eventually, the entire planning procedure could be performed using a trained machine learning algorithm. The plan would still require an expert reader to ensure the efficacy of the plan, and would require a massive amount of training data for proper model development, so the replacement of the medical dosimetrist in treatment planning by a robot will not be happening anytime soon. Advantages to the

atlas-based method would be that there would not be a massive requirement of data such as in the case of the machine learning based methods. Additionally, the temporal efficiency of an atlas-based method should be better, as the processing requirements are less versus something like a convolutional neural network.

Additional future work should be carried out to correct for the general overestimation of the breast radius and separation by the Hough transform when the actual radius and separation values go below 5 cm and 14 cm respectively. This is shown in Figure 15, and is typically seen in the far superior and inferior regions of the treatment volume. There are several ways to address this overestimation, the simplest of which would be to apply a multiplicative weighting factor to the minor and major axes lengths following the conversion from number of pixels to a length in centimeters. This would be a simple scaling of the breast radius and separation estimation to bring it closer to the actual radius and separation measurement. It would only be used towards the superior and inferior portions of the treatment volume, which are the regions where the estimation appears to have a general bias to overestimate the true breast radius and separation. Such a weighting would then prevent the potential overdosing of these regions due to the thickness of the breast being overestimated by the algorithm. This causes the generated fluence map to be too high in those regions. The weighting factor could also be applied to the fluence map, but it would be more difficult to debug in that case. It is easier to assess the corrected radius and separation estimation against the true measurement than it would be to check the two dose distributions for regions of overdosing and a potential drop in dose homogeneity throughout the treatment volume.

There are other portions of the electronic compensation treatment planning procedure that might be improved with some automation. A radiation oncologist typically contours the breast treatment volume and the surrounding tissue and critical organs such as the heart and lungs. This is a very manual process that requires lots of attention which may contribute to some of the physician burnout often reported in this day and age[116]. This type of a problem is well-posed for a convolutional neural network due to the vast amount of organ contours already present, and has been the topic of lots of development and research in the previous years[117,118]. We predict that it will not be long until the treatment planning software will include some levels of automation for organ segmentation, treatment planning, or even something like treatment outcome prediction using convolutional neural networks or some other machine learning framework.

4.2 – Project Conclusions

The work that was completed over the course of this thesis was primarily involved with the development of a more automated framework for electronic compensation breast cancer treatment planning. The hypothesis at the onset of this project was that the breast radius and separation measurement could be correlated to the optimal x-ray beam fluence needed to deliver the most homogenous dose distribution throughout the treatment volume. This is not a novel idea, other work has been published which has investigated the potential of this correlation. What was novel was our use of the entire breast volume for this correlation, instead of just a single or a few measurements of breast radius and separation. A two-faceted algorithm (entire MATLAB programming code found in Appendix A) was developed for this work; the first portion for the estimation of the breast radius and separation using preprocessing of pre-treatment CT-simulation image

data in conjunction with the Hough transform, the second portion for the correlation of the radius and separation measurements with the beam fluence required to deliver the homogenously optimal treatment to the breast volume. Following the development of this algorithm, we comprehensively assessed it in several ways. The breast radius and separation portion was compared against hand-measurements of breast radius and separation over three collected CT-simulation image datasets for average percent difference between the two. The entire processing framework's generated plans were compared with the original delivered plans manually generated by the medical dosimetrist using institutional dose constraints and the dose homogeneity index. Additional comparisons were carried out against two other semi-supervised methods for treatment plan generation reported in the literature, assuming a single or three compensation depths throughout the breast volume. Treatment plan comparisons were done using ten collected electronic compensation treatment courses. Our results indicated that our algorithm could semi-automatically estimate the breast radius and separation throughout the entire treatment volume with good agreement with the hand-measurements (less than 1 cm difference averaged over 3 collected breast volumes), although there were examples of overestimation of breast radius and separation in the case of small breast sizes towards the volume periphery. Considering the treatment courses, our algorithm's treatment plans were able to approach the performance of the medical dosimetrist plans in terms of the dose homogeneity and the dose constraints. There was no statistical difference between the HI, averaged over the test cohort, of our algorithm's plans and those from the medical dosimetrist, and dose constraints were met equally by the two sets of plans. Our algorithm does this with much less manual supervision required and in

much less time compared with the iterative and manual process of the current clinical standard method. Our algorithm was able to improve on the other semi-supervised techniques in terms of the deliverability of the plans due to institutional dose constraints as well as the dose homogeneity index (HI 12.6 vs 15.6 vs 17.0 for our plans, the three-region breast model, and the single TPD model respectively). This indicates that utilizing the breast radius and separation measurements over the entire breast volume can lead to the generation of improved treatment plans, at least in the limited data cohort that this work was assessed using.

We picture an algorithm such as this fitting into the clinical workflow as a 'closer to clinically deliverable' starting point for the iterative process of the medical dosimetrist. This algorithm, which considers the variation in breast radius and separation in the cranio-caudal direction, generated plans that are more homogenous and closer to deliverable in terms of dose constraints than those plans generated considering only one or a few measurements of the breast radius and separation, ignoring the variation in the cranio-caudal direction. A medical dosimetrist starting from plans generated from our algorithm might have fewer iterations of manually editing the fluence maps needed compared with starting from the current standard of plans generated assuming a single compensation depth. This improves the clinical workflow, and reduces some of the variability associated with the current forward-planning procedure.

Work such as this is important for the development of more tools that aid in the radiation therapy treatment planning room. Such tools may reduce variability between planners, improve the clinical workflow of the planning process, or even aid in the decision making which takes place during treatment planning. All of this is beneficial to the patient

undergoing the treatment, and any tool used prior to or during the treatment must keep the patient's best interests as the top priority.

Appendix A – MATLAB Algorithm Used in Project

Included in this appendix is the code used for this work, a flowchart explaining the flow of data through the various processing, and a user-guide giving more detail to certain steps.

Appendix A.1 – User Guide for MATLAB Algorithm

1. User selects the directory containing the DICOM image data from a popup window. This assumes that each individual slice is an individual file within the directory. DICOM files read in based on axial position, so they are ordered correctly within the stack.

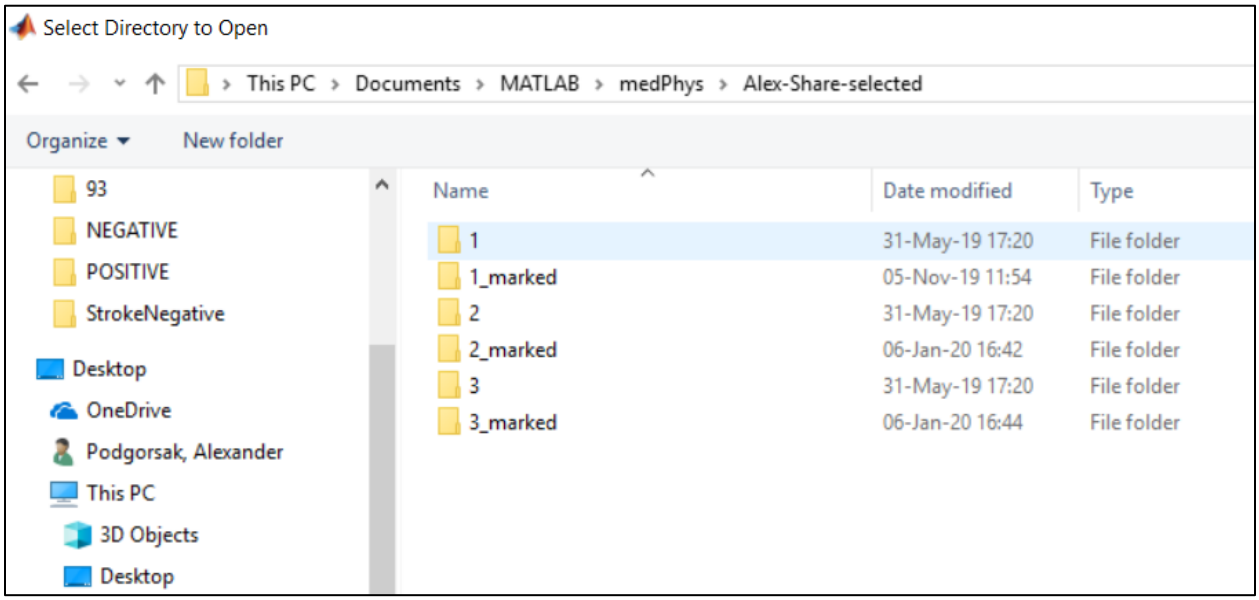

2. Central slice of the CT-simulation data is displayed and the user defines two ROIs corresponding to regions where the medial and ipsilateral markers can be found. This is the only supervision required by the program, and is how the sidedness of the treatment

is determined. If the medial marker's x-position is to the right of the ipsilateral marker, it is a right sided treatment, otherwise it is left sided. Instructions are included in the MATLAB command window to guide the user. The ipsilateral marker region is defined first, followed by the medial marker region. These markers are defined by selecting a square ROI around the markers, top left corner first followed by the bottom right corner. The image data within the ROI is used to isolate the markers away from any image artifacts such that intensity thresholding can be used for marker identification. These markers are visible for multiple axial slices, so there will be a slice where both markers are present and can be used for the identification.

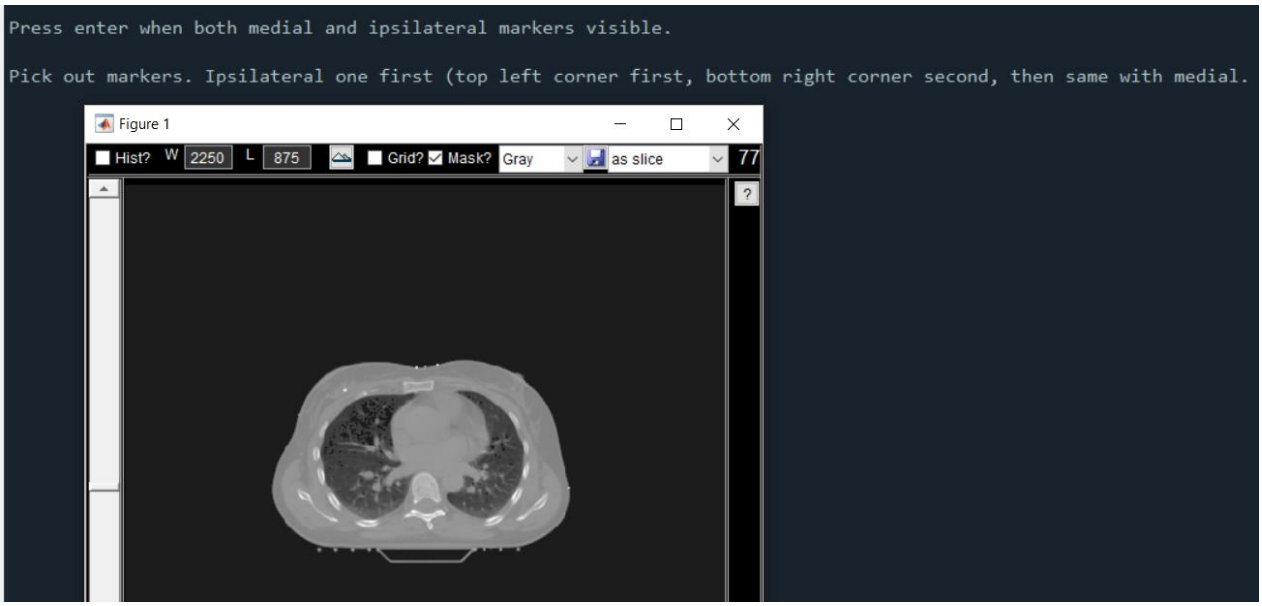

3. Marker positions used to remove all but the breast from the image data. This is put to the elliptical Hough transform where the breast radius and separation are estimated.

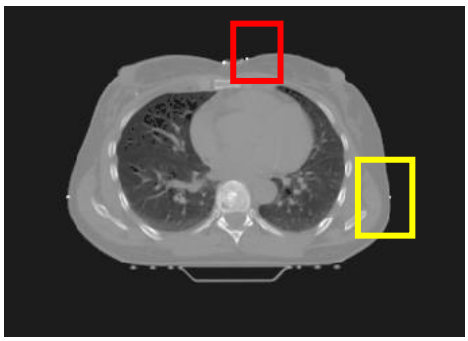

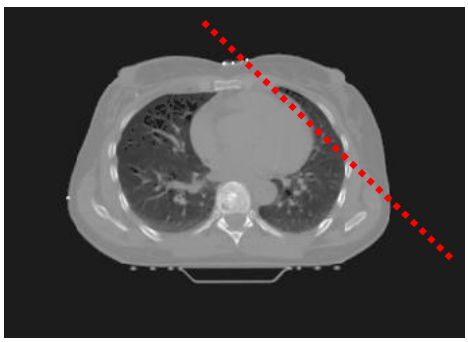

4. Each slice within the treatment volume is put to the elliptical Hough transform. The treatment volume is empirically defined as being within the middle 30% of the CT-simulation data (between the 35% and 65% position axially through the CT-simulation stack). This was determined through some trial and error, but it encompasses the superior and inferior markers and the fluence maps output from this processing are sized appropriately for Eclipse treatment planning software, which our institution uses. The CT-simulation stack length will depend on the size of the breast, so we can change how many slices we consider as the treatment volume taking into account the patient specifics. A

```
for z = ceil(3.5*numel(infos)/10):floor(6.5*numel(infos)/10) % this one
    substack = stack(:,:,z);
    substack(mask) = 0; % apply mask on entire stack
    substack = bwareaopen(substack, 100); % remove small things from the

    ellipse = regionprops(substack,{'MajorAxisLength', 'MinorAxisLength'

%     slice(n) = z;
    sep(n) = ellipse(1).MajorAxisLength*sf/10.0;
    rad(n) = ellipse(1).MinorAxisLength*sf/10.0; % extraction of the sep
```

morphological opening is used to remove any small spurious objects from the image data prior to the Hough transform. The radius and separation are estimated then put to the mathematical model correlating the optimal beam fluence with the size measurements for all of the beam energies regardless of what was used for the treatment.

5. This optimal fluence map is two-dimensional, and has a header containing the information Eclipse needs to read the map into the treatment planning software. This information includes the matrix size in the number of pixels in the x and y direction, the size of those pixels in centimeters to convert to a real distance, and the fluence map origin location. The rest of the information in the fluence file is the individual fluence factors at each pixel.

```
#
#
OptimalFluence
SizeX          80
SizeY          80
SpacingX      2.50
SpacingY      2.50
OriginX       -100
OriginY        100
Values
 0.5000802  0.4967189  0.4905564  0.4883156  0.489996
0.4614499  0.4617524  0.4617524  0.4555916  0.4530708
0.4334629  0.4334629  0.4334629  0.4334629  0.4334629
 0.4239678  0.4172451  0.4290098  0.4256485  0.419486
 0.4289812  0.4256198  0.4256198  0.4256198  0.425619
```

6. Maps for both the medial and ipsilateral x-ray fields are generated with this process. To ensure that the locations match up between the two fields, the fluence maps are first computed from the ipsilateral direction where the superior section of the map corresponds to the superior section of the breast volume. The ipsilateral map is then rotated 270°, then flipped over its x-axis to reorient the map correctly. These two maps are saved as 'optimal_fluence' files, which can be taken as input by Eclipse for treatment planning.

Appendix A.2 – MATLAB Computer Code

```
% written by ARP 2/2019

clear all, close all, clc


%// Get all of the files

directory = uigetdir();

files = dir(fullfile(directory, '*.dcm'));

filenames = cellfun(@(x)fullfile(directory, x), {files.name}, 'uni', 0);


%// Ensure that they are actually DICOM files and remove the ones that aren't

notdicom = ~cellfun(@isdicom, filenames);

files(notdicom) = [];


%// Now load all the DICOM headers into an array of structs

infos = cellfun(@dicominfo, filenames);


%// Now sort these by the instance number

[~, inds] = sort([infos.InstanceNumber]);

infos = infos(inds);


%// read in stack of dicoms in correct order

for k = 1:numel(infos)

    stack(:,:,k) = dicomread(infos(k));
```

```
    substack2 = stack(:,:,k);
    mask2 = imbinarize(substack2, 'global');
    mask2 = bwareaopen(mask2, 10000);

    % figure, imagesc(mask);
    substack2(~mask2) = 0; % apply mask
    stack(:,:,k) = substack2;
end

fprintf('\nPress enter when both medial and ipsilateral markers visible.\n');
tool = imtool3D(stack);
setCurrentSlice(tool,ceil(size(stack,3)/2));
setDisplayRange(tool,[-250 2000]);
pause
mid = stack(:,:,getCurrentSlice(tool));

fprintf('\nPick out markers. Ipsilateral one first (top left corner first, bottom right corner second, then same with medial.\n');
figure, imagesc(mid), hold on;
[ipsilateralX1,ipsilateralY1,~] = ginput(1);
[ipsilateralX2,ipsilateralY2,~] = ginput(1);

ipsilateralY1=round(ipsilateralY1);
```

```
ipsilateralX1=round(ipsilateralX1);
ipsilateralY2=round(ipsilateralY2);
ipsilateralX2=round(ipsilateralX2);

ipsilateralBox =
mid(min(ipsilateralY1,ipsilateralY2):max(ipsilateralY1,ipsilateralY2),min(ipsilateralX1,ipsi
lateralX2):max(ipsilateralX1,ipsilateralX2));
[ipsiX,ipsiY] = find(ipsilateralBox == max(max(ipsilateralBox)));

[medialX1,medialY1,~] = ginput(1);
[medialX2,medialY2,~] = ginput(1);

medialY1=round(medialY1);
medialX1=round(medialX1);
medialY2=round(medialY2);
medialX2=round(medialX2);

medialBox =
mid(min(medialY1,medialY2):max(medialY1,medialY2),min(medialX1,medialX2):max(m
edialX1,medialX2));
[mediX,mediY] = find(medialBox == max(max(medialBox)));

if ipsilateralX2 < medialX2
```

```
    % % left-sided treatment
    ipsiX = ipsilateralX1 + ipsiX; % actual X coordinate of ipsilateral marker
    ipsiY = ipsiY + ipsilateralY1; % actual Y coordinate of ipsilateral marker
    mediX = medialX1 + mediX; % actual X coordinate of ipsilateral point
    mediY = mediY + medialY1; % actual Y coordinate of ipsilateral point
    plane = interp1([mediX ipsiX],[mediY ipsiY], 1:512, 'linear', 'extrap');
    plane = int16(max(1,plane)); % restrict to a maximum value of 1 for looping later
    plot(plane, '--k');
    for x = 1:512
        if plane(x) == 1
            down = x;
            break
        else
            down = 512;
        end
    end
    mask = poly2mask(double([1 down 1 1]), double([1 1 plane(1) 1]), size(mid,1),
size(mid,2));    % if a left-sided treatment
    mask = ~mask; % for left-sided treatment
else
    % % right-sided treatment
    ipsiX = ipsilateralX2 - ipsiX; % actual X coordinate of ipsilateral marker
    ipsiY = ipsiY + ipsilateralY1; % actual Y coordinate of ipsilateral marker
```

```
    mediX = medialX2 - mediX; % actual X coordinate of ipsilateral point
    mediY = mediY + medialY1; % actual Y coordinate of ipsilateral point
    plane = interp1([mediX ipsiX],[mediY ipsiY], 1:512, 'linear', 'extrap');
    plane = int16(max(1,plane)); % restrict to a maximum value of 1 for looping later
    plot(plane, '--k');
    for x = 1:512
        if plane(x) > 1
            down = x;
            break
        end
    end
    mask = poly2mask(double([1 down-1 size(mid,1) size(mid,1) 1 1]), double([1 1
plane(numel(plane)) size(mid,2) size(mid,2) 1]), size(mid,1), size(mid,2));    % if a right-
sided treatment
end

figure, imagesc(mask);
%// extract pixelsize for scaling factor [conversion from pixels to mm then
%// to cm
sf = infos(1).PixelSpacing(1);

attenuation_const = 1; % constant scaling factor in the transmittance computation
```

```
dist_scaling = 250; % a distance scaling factor for the radiation transmittance through the phantom
total = 50; % total number of samples in the fluence map
n = 1;

for z = ceil(3.5*numel(infos)/10):floor(6.5*numel(infos)/10) % this one is for compuation of the size/shape slice by slice
    substack = stack(:,:,z);
    substack(mask) = 0; % apply mask on entire stack
    substack = bwareaopen(substack, 100); % remove small things from the image one last time

    ellipse = regionprops(substack,{'MajorAxisLength', 'MinorAxisLength', 'Orientation', 'Centroid'}); % extract the seperation and the radius

%     slice(n) = z;
    sep(n) = ellipse(1).MajorAxisLength*sf/10.0;
    rad(n) = ellipse(1).MinorAxisLength*sf/10.0; % extraction of the separation and radius of breast measured in pixels

%     % additionally do TPD using alf's model and show how that changes with the cranio-caudal direction
%     if rad(n) > 6.0 || rad(n) < 10.0
```

```
%       TPD(n) = -1.30 * sep(n) + 55;
%   elseif rad(n) <= 6.0
%       TPD(n) = -1.34 * sep(n) + 59;
%   elseif rad(n) >= 10.0
%       TPD(n) = -1.20 * sep(n) + 48;
%   end

%   a = ellipse(1).MajorAxisLength/2;
%   b = ellipse(1).MinorAxisLength/2;
%
%   fig = imagesc(stack(:,:,z));
%   colormap gray
%   hold on
%
%   xbar = ellipse(1).Centroid(1);
%   ybar = ellipse(1).Centroid(2);
%
%   theta = pi*ellipse(1).Orientation/180;
%   R = [ cos(theta)   sin(theta)
%        -sin(theta)   cos(theta)];
%
%   phi = linspace(0,2*pi,50);
%   cosphi = cos(phi);
```

```
%     sinphi = sin(phi);
%
%     xy = [a*cosphi; b*sinphi];
%     xy = R*xy;
%
%     x = xy(1,:) + xbar;
%     y = xy(2,:) + ybar;
%
%     plot(x,y,'r','LineWidth',2);
%     sep_str = strcat('Sep = ', int2str(sep));
%     rad_str = strcat('Rad = ', int2str(rad));
%     text(45,45,sep_str, 'Color','yellow', 'Fontsize',12);
%     text(45,70,rad_str, 'Color','yellow', 'Fontsize',12);
%     hold off
%       saveas(fig, strcat('C:\Users\arpodgor\Documents\MATLAB\medPhys\Alex-Share-selected\3_marked\slice_',int2str(z),'.png'));
   % convert to mm by pulling the scaling factor from the dicom tags then multiplying
%     sep_cm(z-ceil(numel(infos)/4)+1) = sep*sf/10.;
%     rad_cm(z-ceil(numel(infos)/4)+1) = rad*sf/10.; % measurements in cm


   TF(1,n) = 0.753 + 0.006*rad(n) - 0.005*sep(n); % for a 6x beam
   for depth = 2:total % splitting up the fluence map into 100 samples, this can and probably will have to be changed to match what eclipse wants
```

% now estimate how the radiation intensity will drop as it moves through the phantom (Beer-Lambert Law)

TF(depth,n) = TF(1,n) * exp((-attenuation_const*depth/dist_scaling)); % the scaling factor will also be changed

end

% TF(1,z-ceil(3.5*numel(infos)/10)+1) = 0.8318 + 0.0101*rad - 0.0057*sep; % for a 10x beam

% for depth = 2:total % splitting up the fluence map into 100 samples, this can and probably will have to be changed to match what eclipse wants

% % now estimate how the radiation intensity will drop as it moves through the phantom (Beer-Lambert Law)

% TF(depth,z-ceil(3.5*numel(infos)/10)+1) = TF(1,z-ceil(3.5*numel(infos)/10)+1) * exp((-attenuation_const*depth/dist_scaling)); % the scaling factor will also be changed

% end

%

TF(1,z-ceil(3.5*numel(infos)/10)+1) = 0.8878 + 0.0061*rad - 0.0068*sep; % for a 23x beam

for depth = 2:total % splitting up the fluence map into 100 samples, this can and probably will have to be changed to match what eclipse wants

% now estimate how the radiation intensity will drop as it moves through the phantom (Beer-Lambert Law)

```
        TF(depth,z-ceil(3.5*numel(infos)/10)+1)  =  TF(1,z-ceil(3.5*numel(infos)/10)+1)  *
exp((-attenuation_const*depth/dist_scaling)); % the scaling factor will also be changed
    end
    n = n + 1; % slice counter
end

tot = floor(6.5*numel(infos)/10) - ceil(3.5*numel(infos)/10);
for z = ceil(3.5*numel(infos)/10):floor(6.5*numel(infos)/10) % this one is for the alghufali
method
    substack = stack(:,:,z);
    substack(mask) = 0; % apply mask on entire stack
    substack = bwareaopen(substack, 100); % remove small things from the image one
last time

    ellipse  =  regionprops(substack,{'MajorAxisLength',  'MinorAxisLength',  'Orientation',
'Centroid'}); % extract the seperation and the radius

    sep(n) = ellipse(1).MajorAxisLength*sf/10.0;
    rad(n) = ellipse(1).MinorAxisLength*sf/10.0;

    n = n + 1; % slice counter
end
```

```
% tot = floor(6.5*numel(infos)/10) - ceil(3.5*numel(infos)/10);

avg_sep_sup = mean(sep(1:floor(tot/3)));
avg_rad_sup = mean(rad(1:floor(tot/3)));

avg_sep_mid = mean(sep(ceil(tot/3):floor(2*tot/3)));
avg_rad_mid = mean(rad(ceil(tot/3):floor(2*tot/3)));

avg_sep_inf = mean(sep(ceil(2*tot/3):end));
avg_rad_inf = mean(rad(ceil(2*tot/3):end));

n = 1;
for z = ceil(3.5*numel(infos)/10):floor(6.5*numel(infos)/10)
    if z < ceil(3.5*numel(infos)/10) + floor(tot/3) % superior most third
        TF(1,n) = 0.753 + 0.006*avg_rad_sup - 0.005*avg_sep_sup; % for a 6x beam
        for depth = 2:total % splitting up the fluence map into 100 samples, this can and probably will have to be changed to match what eclipse wants
        % now estimate how the radiation intensity will drop as it moves through the phantom (Beer-Lambert Law)
            TF(depth,n) = TF(1,n) * exp((-attenuation_const*depth/dist_scaling)); % the scaling factor will also be changed
        end
```

```
%                TF(1,z-ceil(3.5*numel(infos)/10)+1) = 0.8878 + 0.0061*avg_rad_sup -
0.0068*avg_sep_sup; % for a 23x beam
%        for depth = 2:total % splitting up the fluence map into 100 samples, this can and
probably will have to be changed to match what eclipse wants
%             % now estimate how the radiation intensity will drop as it moves through the
phantom (Beer-Lambert Law)
%             TF(depth,z-ceil(3.5*numel(infos)/10)+1) = TF(1,z-ceil(3.5*numel(infos)/10)+1)
* exp((-attenuation_const*depth/dist_scaling)); % the scaling factor will also be changed
%        end

   elseif (z >= ceil(3.5*numel(infos)/10) + floor(tot/3)) && (z < ceil(3.5*numel(infos)/10) +
floor(2*tot/3)) % middle third
       TF(1,n) = 0.753 + 0.006*avg_rad_mid - 0.005*avg_sep_mid; % for a 6x beam
       for depth = 2:total % splitting up the fluence map into 100 samples, this can and
probably will have to be changed to match what eclipse wants
       % now estimate how the radiation intensity will drop as it moves through the phantom
(Beer-Lambert Law)
           TF(depth,n) = TF(1,n) * exp((-attenuation_const*depth/dist_scaling)); % the
scaling factor will also be changed
       end

%                TF(1,z-ceil(3.5*numel(infos)/10)+1) = 0.8878 + 0.0061*avg_rad_mid -
0.0068*avg_sep_mid; % for a 23x beam
```

```
%       for depth = 2:total % splitting up the fluence map into 100 samples, this can and probably will have to be changed to match what eclipse wants
%           % now estimate how the radiation intensity will drop as it moves through the phantom (Beer-Lambert Law)
%           TF(depth,z-ceil(3.5*numel(infos)/10)+1) = TF(1,z-ceil(3.5*numel(infos)/10)+1) * exp((-attenuation_const*depth/dist_scaling)); % the scaling factor will also be changed
%       end

    else % inferior most third
        TF(1,n) = 0.753 + 0.006*avg_rad_inf - 0.005*avg_sep_inf; % for a 6x beam
        for depth = 2:total % splitting up the fluence map into 100 samples, this can and probably will have to be changed to match what eclipse wants
        % now estimate how the radiation intensity will drop as it moves through the phantom (Beer-Lambert Law)
            TF(depth,n) = TF(1,n) * exp((-attenuation_const*depth/dist_scaling)); % the scaling factor will also be changed
        end

%           TF(1,z-ceil(3.5*numel(infos)/10)+1) = 0.8878 + 0.0061*avg_rad_inf - 0.0068*avg_sep_inf; % for a 23x beam
%       for depth = 2:total % splitting up the fluence map into 100 samples, this can and probably will have to be changed to match what eclipse wants
```

```
%            % now estimate how the radiation intensity will drop as it moves through the
phantom (Beer-Lambert Law)
%            TF(depth,z-ceil(3.5*numel(infos)/10)+1) = TF(1,z-ceil(3.5*numel(infos)/10)+1)
* exp((-attenuation_const*depth/dist_scaling)); % the scaling factor will also be changed
%        end
    end
    n = n + 1; % slice counter
end

avg_sep = mean(sep);
avg_rad = mean(rad);

n = 1;
for z = ceil(3.5*numel(infos)/10):floor(6.5*numel(infos)/10)

    TF(1,n) = 0.753 + 0.006*avg_rad - 0.005*avg_sep; % for a 6x beam
    for depth = 2:total % splitting up the fluence map into 100 samples, this can and
probably will have to be changed to match what eclipse wants
        % now estimate how the radiation intensity will drop as it moves through the phantom
(Beer-Lambert Law)
        TF(depth,n) = TF(1,n) * exp((-attenuation_const*depth/dist_scaling)); % the scaling
factor will also be changed
    end
```

```
    n = n + 1; % slice counter
end

% pass the vectors through a median filter, we can assume no huge changes from slice
to slice in the size/shape
sep_med = medfilt1(sep, 7);
rad_med = medfilt1(rad, 7);
TPD_med = medfilt1(TPD, 7);

% plot of the breast separation and radius estimation slice by slice
% figure
% plot(sep, 'Color', 'k')
% xlabel('Axial slice number')
% ylabel('Breast separation (cm)')
%
% figure
% plot(rad, 'Color', 'k')
% xlabel('Axial slice number')
% ylabel('Breast radius (cm)')
%
% figure
% plot(TPD, 'Color', 'k')
```

```
% xlabel('Axial slice number')
% ylabel('Optimal TPD')

figure
plot(sep_med, 'Color', 'k')
xlabel('Axial slice number')
ylabel('Breast separation (cm)')

figure
plot(rad_med, 'Color', 'k')
xlabel('Axial slice number')
ylabel('Breast radius (cm)')

TPD_alf = zeros(1,n-1);
TPD_alf(1:20) = mean(TPD(1:20));
TPD_alf(21:40) = mean(TPD(21:40));
TPD_alf(41:n-1) = mean(TPD(41:n-1));

TPD_const = zeros(1,n-1);
TPD_const(:) = 30;

figure
hold on;
```

```
plot(TPD_med, 'Color', 'k')

plot(TPD_alf, 'Color', 'b')

plot(TPD_const, 'Color', 'g')

xlabel('Axial slice number')

ylabel('Optimal TPD (%)')

legend('Continuous model', '3-region breast model', 'Single TPD')

hold off;


figure

plot(TF(1,:), 'Color', 'k')

xlabel('Axial slice number')

ylabel('Surface Fluence')

% figure, imagesc(TF);
```

Appendix A.3 – Flow Chart for Project

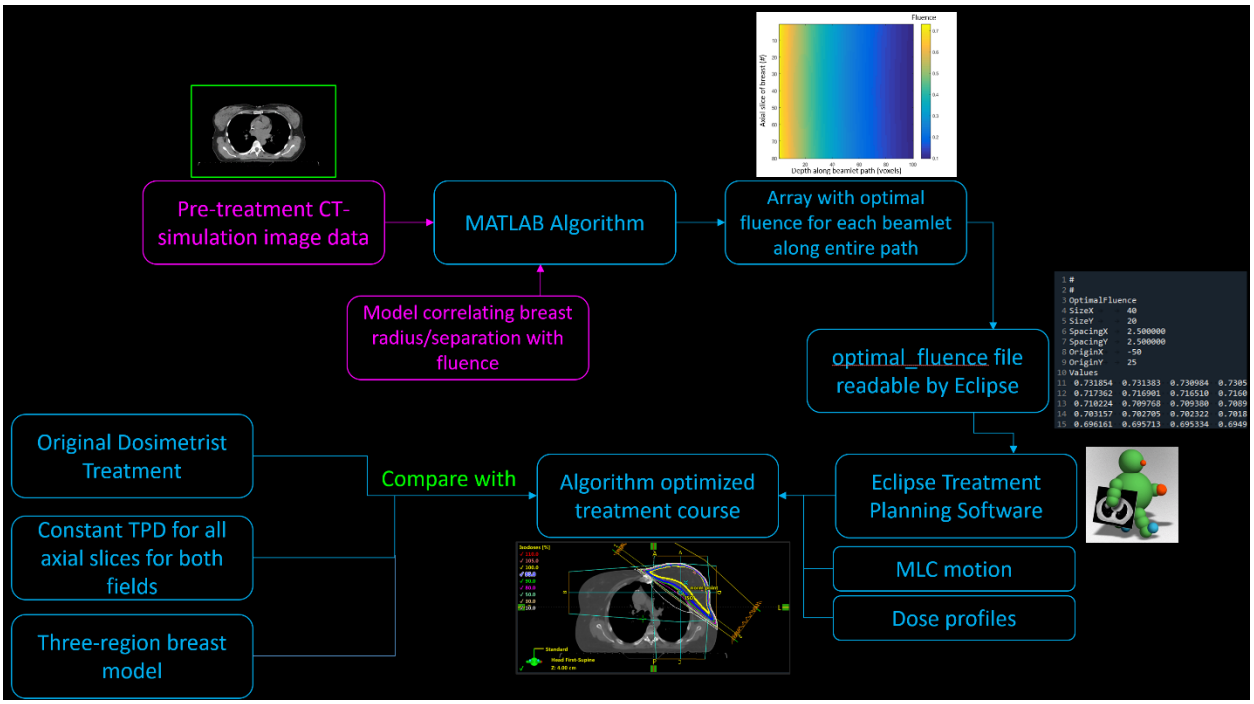

Appendix A.4 – Flow Chart for Algorithm

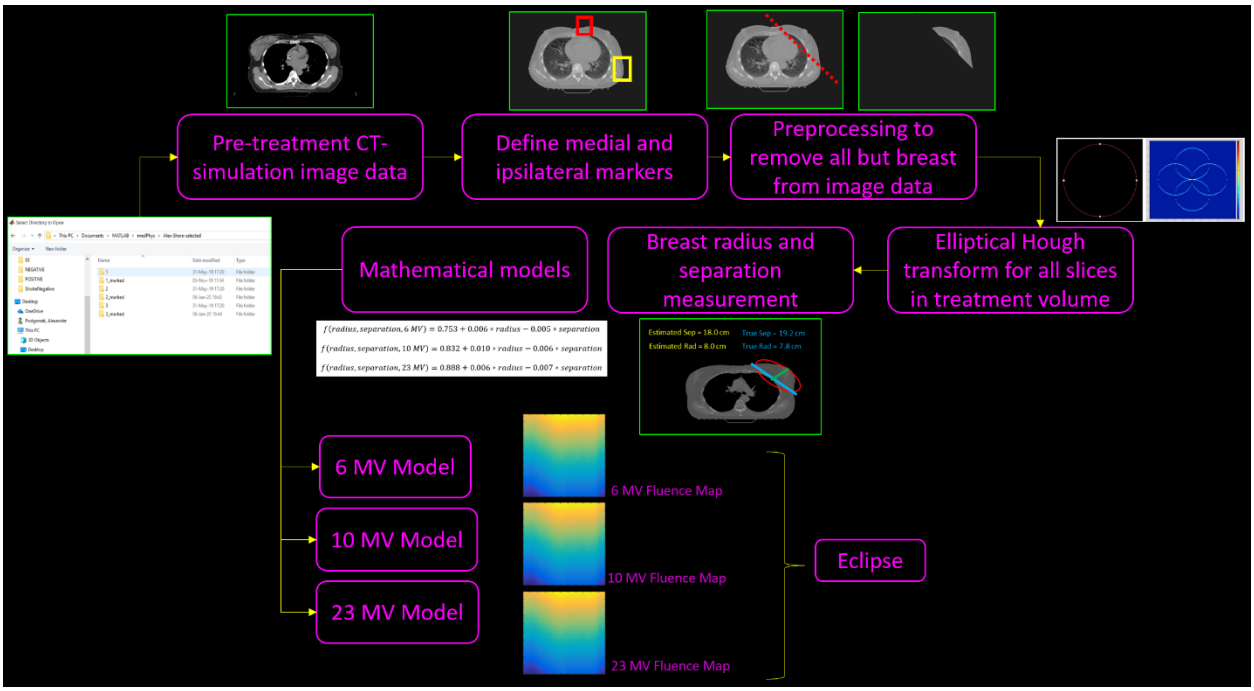

Bibliography

1. Siegel RL, Miller KD, Jemal A. Cancer statistics, 2020. *CA: A Cancer Journal for Clinicians.* 2020;70(1):7-30.
2. Waks AG, Winer EP. Breast Cancer Treatment: A Review. *JAMA.* 2019;321(3):288-300.
3. Ahn S, Wooster M, Valente C, et al. Impact of Screening Mammography on Treatment in Women Diagnosed with Breast Cancer. *Annals of Surgical Oncology.* 2018;25(10):2979-2986.
4. Pisano ED, Yaffe MJ. Digital mammography. *Radiology.* 2005;234(2):353-362.
5. Mandelblatt JS, Cronin KA, Bailey S, et al. Effects of mammography screening under different screening schedules: model estimates of potential benefits and harms. *Annals of internal medicine.* 2009;151(10):738-747.
6. Yaffe MJ, Mainprize JG. Risk of radiation-induced breast cancer from mammographic screening. *Radiology.* 2011;258(1):98-105.
7. Kriege M, Brekelmans CT, Boetes C, et al. Efficacy of MRI and mammography for breast-cancer screening in women with a familial or genetic predisposition. *New England Journal of Medicine.* 2004;351(5):427-437.
8. Berg WA, Zhang Z, Lehrer D, et al. Detection of breast cancer with addition of annual screening ultrasound or a single screening MRI to mammography in women with elevated breast cancer risk. *Jama.* 2012;307(13):1394-1404.
9. Skaane P, Bandos AI, Gullien R, et al. Comparison of digital mammography alone and digital mammography plus tomosynthesis in a population-based screening program. *Radiology.* 2013;267(1):47-56.
10. Haas BM, Kalra V, Geisel J, Raghu M, Durand M, Philpotts LE. Comparison of tomosynthesis plus digital mammography and digital mammography alone for breast cancer screening. *Radiology.* 2013;269(3):694-700.
11. Alimirzaie S, Bagherzadeh M, Akbari MR. Liquid biopsy in breast cancer: A comprehensive review. *Clinical genetics.* 2019;95(6):643-660.
12. Skeel RT, Khleif SN. *Handbook of cancer chemotherapy.* Lippincott Williams & Wilkins; 2011.
13. Kennedy SP, Han JZ, Portman N, et al. Targeting promiscuous heterodimerization overcomes innate resistance to ERBB2 dimerization inhibitors in breast cancer. *Breast Cancer Research.* 2019;21(1):43.
14. Prado CM, Baracos VE, McCargar LJ, et al. Sarcopenia as a determinant of chemotherapy toxicity and time to tumor progression in metastatic breast cancer patients receiving capecitabine treatment. *Clinical cancer research.* 2009;15(8):2920-2926.
15. Steward LT, Gao F, Taylor MA, Margenthaler JA. Impact of radiation therapy on survival in patients with triple-negative breast cancer. *Oncology letters.* 2014;7(2):548-552.
16. Yagata H, Kajiura Y, Yamauchi H. Current strategy for triple-negative breast cancer: appropriate combination of surgery, radiation, and chemotherapy. *Breast Cancer.* 2011;18(3):165-173.
17. Zhao H, Zhuang Y, Li R, et al. Effects of different doses of X-ray irradiation on cell apoptosis, cell cycle, DNA damage repair and glycolysis in HeLa cells [published online ahead of print 2018/10/11]. *Oncology letters.* 2019;17(1):42-54.
18. Hoskin P, Coyle C. *Radiotherapy in Practice - Brachytherapy.* doi: 10.1093/med/9780199600908.001.0001: Oxford University Press; 2013.
19. Smith GL, Xu Y, Buchholz TA, et al. Association Between Treatment With Brachytherapy vs Whole-Breast Irradiation and Subsequent Mastectomy, Complications, and Survival Among Older Women With Invasive Breast Cancer. *JAMA.* 2012;307(17):1827-1837.

20. Smith BD, Arthur DW, Buchholz TA, et al. Accelerated Partial Breast Irradiation Consensus Statement From the American Society for Radiation Oncology (ASTRO). *International Journal of Radiation Oncology*Biology*Physics.* 2009;74(4):987-1001.
21. Buchholz TA. Partial breast irradiation—is it ready for prime time? *International Journal of Radiation Oncology*Biology*Physics.* 2003;57(5):1214-1216.
22. Clark R, Whelan T, Levine M, et al. Randomized clinical trial of breast irradiation following lumpectomy and axillary dissection for node-negative breast cancer: an update. *JNCI: Journal of the National Cancer Institute.* 1996;88(22):1659-1664.
23. Fisher B, Anderson S, Bryant J, et al. Twenty-year follow-up of a randomized trial comparing total mastectomy, lumpectomy, and lumpectomy plus irradiation for the treatment of invasive breast cancer. *New England Journal of Medicine.* 2002;347(16):1233-1241.
24. Forrest AP, Stewart HJ, Everington D, et al. Randomised controlled trial of conservation therapy for breast cancer: 6-year analysis of the Scottish trial. *The Lancet.* 1996;348(9029):708-713.
25. Veronesi U, Luini A, Del Vecchio M, et al. Radiotherapy after breast-preserving surgery in women with localized cancer of the breast. *New England Journal of Medicine.* 1993;328(22):1587-1591.
26. Curran D, Van Dongen J, Aaronson NK, et al. Quality of life of early-stage breast cancer patients treated with radical mastectomy or breast-conserving procedures: results of EORTC Trial 10801. *European Journal of Cancer.* 1998;34(3):307-314.
27. Powell S, Cooke J, Parsons C. Radiation-induced brachial plexus injury: follow-up of two different fractionation schedules. *Radiotherapy and Oncology.* 1990;18(3):213-220.
28. Ash D, Benson E, Sainsbury J, Round C, Head C. Seven-year follow-up on 334 patients treated by breast conserving surgery and short course radical postoperative radiotherapy: a report of the Yorkshire Breast Cancer Group. *Clinical Oncology.* 1995;7(2):93-96.
29. Olivotto IA, Weir LM, Kim-Sing C, et al. Late cosmetic results of short fractionation for breast conservation. *Radiotherapy and oncology.* 1996;41(1):7-13.
30. Shelley W, Brundage M, Hayter C, Paszat L, Zhou S, Mackillop W. A shorter fractionation schedule for postlumpectomy breast cancer patients. *International Journal of Radiation Oncology* Biology* Physics.* 2000;47(5):1219-1228.
31. Fowler JF. The linear-quadratic formula and progress in fractionated radiotherapy. *The British journal of radiology.* 1989;62(740):679-694.
32. Virnig B, Habermann E, Al-Refaie W, Jensen E, Tuttle T. Increased use of breast-conserving surgery: Preferred treatment or failure to provide adequate local therapy? *Breast Cancer Research and Treatment.* 2007;106.
33. Johansen S, Danielsen T, Rune Olsen D. Estimated risk for secondary cancer in the contra-lateral breast following radiation therapy of breast cancer. *Acta Oncologica.* 2008;47(3):391-396.
34. Darby SC, Ewertz M, McGale P, et al. Risk of ischemic heart disease in women after radiotherapy for breast cancer. *New England Journal of Medicine.* 2013;368(11):987-998.
35. Alford SL, Prassas GN, Vogelesang CR, Leggett HJ, Hamilton CS. Adjuvant breast radiotherapy using a simultaneous integrated boost: clinical and dosimetric perspectives. *Journal of medical imaging and radiation oncology.* 2013;57(2):222-229.
36. Menard J, Campana F, Kirov K, et al. Radiotherapy for breast cancer and pacemaker. *Cancer radiotherapie: journal de la Societe francaise de radiotherapie oncologique.* 2011;15(3):197-201.
37. Smith BD, Haffty BG, Wilson LD, Smith GL, Patel AN, Buchholz TA. The future of radiation oncology in the United States from 2010 to 2020: will supply keep pace with demand? *Journal of clinical oncology.* 2010;28(35):5160-5165.
38. Correa CR, Litt HI, Hwang W-T, Ferrari VA, Solin LJ, Harris EE. Coronary artery findings after left-sided compared with right-sided radiation treatment for early-stage breast cancer. *Journal of clinical oncology.* 2007;25(21):3031-3037.

39. Harris EE, Correa C, Hwang W-T, et al. Late cardiac mortality and morbidity in early-stage breast cancer patients after breast-conservation treatment. *Journal of clinical oncology.* 2006;24(25):4100-4106.
40. Recht A. Which breast cancer patients should really worry about radiation-induced heart disease—And how much? In.: American Society of Clinical Oncology; 2006.
41. Bartelink H, Horiot J-C, Poortmans PM, et al. Impact of a higher radiation dose on local control and survival in breast-conserving therapy of early breast cancer: 10-year results of the randomized boost versus no boost EORTC 22881-10882 trial. *Journal of Clinical Oncology.* 2007;25(22):3259-3265.
42. Yan L, Xu Y, Chen X, Xie X, Liang B, Dai J. A new homogeneity index definition for evaluation of radiotherapy plans. *Journal of Applied Clinical Medical Physics.* 2019;20(11):50-56.
43. Peulen H, Hanbeukers B, Boersma L, et al. Forward Intensity-Modulated Radiotherapy Planning in Breast Cancer to Improve Dose Homogeneity: Feasibility of Class Solutions. *International Journal of Radiation Oncology*Biology*Physics.* 2012;82(1):394-400.
44. Chui CS, Hong L, Hunt M, McCormick B. A simplified intensity modulated radiation therapy technique for the breast. *Medical physics.* 2002;29(4):522-529.
45. van Asselen B, Raaijmakers CP, Hofman P, Lagendijk JJ. An improved breast irradiation technique using three-dimensional geometrical information and intensity modulation. *Radiotherapy and Oncology.* 2001;58(3):341-347.
46. Donovan E, Bleackley N, Evans P, Reise S, Yarnold J. Dose-position and dose-volume histogram analysis of standard wedged and intensity modulated treatments in breast radiotherapy. *The British journal of radiology.* 2002;75(900):967-973.
47. Goldsmith C, Haviland J, Tsang Y, Sydenham M, Yarnold J. Large breast size as a risk factor for late adverse effects of breast radiotherapy: is residual dose inhomogeneity, despite 3D treatment planning and delivery, the main explanation? *Radiotherapy and Oncology.* 2011;100(2):236-240.
48. Moody A, Mayles W, Bliss J, et al. The influence of breast size on late radiation effects and association with radiotherapy dose inhomogeneity. *Radiotherapy and Oncology.* 1994;33(2):106-112.
49. Bentzen S, Agrawal R, Aird E, et al. The UK Standardisation of Breast Radiotherapy (START) Trial A of radiotherapy hypofractionation for treatment of early breast cancer: a randomised trial. *The Lancet Oncology.* 2008;9(4):331-341.
50. Ahmad M, Hussain A, Muhammad W, Rizvi SQA, Matiullah. Studying wedge factors and beam profiles for physical and enhanced dynamic wedges. *J Med Phys.* 2010;35(1):33-41.
51. Khan FM, Gibbons JP. *Khan's the physics of radiation therapy.* Lippincott Williams & Wilkins; 2014.
52. Eisbruch A, Marsh LH, Martel MK, et al. Comprehensive irradiation of head and neck cancer using conformal multisegmental fields: assessment of target coverage and noninvolved tissue sparing. *International Journal of Radiation Oncology* Biology* Physics.* 1998;41(3):559-568.
53. Galvin JM, Chen X-G, Smith RM. Combining multileaf fields to modulate fluence distributions. *International Journal of Radiation Oncology* Biology* Physics.* 1993;27(3):697-705.
54. Webb S. Configuration options for intensity-modulated radiation therapy using multiple static fields shaped by a multileaf collimator. *Physics in Medicine & Biology.* 1998;43(2):241.
55. Vicini FA, Sharpe M, Kestin L, et al. Optimizing breast cancer treatment efficacy with intensity-modulated radiotherapy. *International Journal of Radiation Oncology* Biology* Physics.* 2002;54(5):1336-1344.
56. ZEEs. Own work. In: MLCShape, ed. Creative Commons: ShareAlike 3.0 Unported; 2008:Field shape of a mult leaf collimator (X-MLC).
57. Chui C-S, Hong L, Hunt M, McCormick B. A simplified intensity modulated radiation therapy technique for the breast. *Medical Physics.* 2002;29(4):522-529.

58. James H, Poynter A, Crosbie J, MacKenzie L, Boston S, LeVay J. Electronic compensation for CT planned breast treatments. *Radiother Oncol.* 2002;64:S133-134.
59. LeVay J, James H, Poynter A, MacKenzie L, Boston S. Optimising the delivery of radiotherapy for early breast cancer by the use of IMRT. *Clin Oncol.* 2003;15:S14.
60. James H, Scrase C, Poynter A. Practical experience with intensity-modulated radiotherapy. *The British journal of radiology.* 2004;77(913):3-14.
61. Mihai A, Rakovitch E, Sixel K, et al. Inverse vs. forward breast IMRT planning. *Medical Dosimetry.* 2005;30(3):149-154.
62. Bär W, Schwarz M, Alber M, et al. A comparison of forward and inverse treatment planning for intensity-modulated radiotherapy of head and neck cancer. *Radiotherapy and Oncology.* 2003;69(3):251-258.
63. Howard M. The incidence of burnout or compassion fatigue in medical dosimetrists as a function of various stress and psychologic factors. *Medical Dosimetry.* 2013;38(1):88-94.
64. Friend M. An overview of Electronic tissue Compensation (ECOMP) for breast Radiotherapy. Conference Poster presented at 2014 Combined Scientific Meeting; 2014, 2014; Vienna, Austria.
65. Emmens D, James H. Irregular surface compensation for radiotherapy of the breast: correlating depth of the compensation surface with breast size and resultant dose distribution. *The British journal of radiology.* 2010;83(986):159-165.
66. Alghufaili AH, Shanmugarajah L, Kumaraswamy LK. Correlating the depth of compensation to the 3-D shape of the breast to achieve homogeneous dose distribution using the electronic tissue compensation treatment technique. *Medical Dosimetry.* 2019;44(1):30-34.
67. Lambert J, Greer PB, Menk F, et al. MRI-guided prostate radiation therapy planning: Investigation of dosimetric accuracy of MRI-based dose planning. *Radiotherapy and Oncology.* 2011;98(3):330-334.
68. Das IJ, Cheng EC, Freedman G, Fowble B. Lung and heart dose volume analyses with CT simulator in radiation treatment of breast cancer. *International Journal of Radiation Oncology*Biology*Physics.* 1998;42(1):11-19.
69. Hiraoka M, Mitsumori M, Okajima K, et al. Use of a CT simulator in radiotherapy treatment planning for breast conserving therapy. *Radiotherapy and Oncology.* 1994;33(1):48-55.
70. Mlynarski P, Delingette H, Alghamdi H, Bondiau P-Y, Ayache N. Anatomically consistent CNN-based segmentation of organs-at-risk in cranial radiotherapy. *Journal of Medical Imaging.* 2020;7(1):014502.
71. Podgorsak AR, Rava RA, Shiraz Bhurwani MM, et al. Automatic radiomic feature extraction using deep learning for angiographic parametric imaging of intracranial aneurysms. *Journal of NeuroInterventional Surgery.* 2019. doi: 10.1136/neurintsurg-2019-015214:neurintsurg-2019-015214.
72. Asano A, Kobayashi Y, Muraki C, Muneyasu M. Optimization of gray scale morphological opening for noise removal in texture images. Paper presented at: The 2004 47th Midwest Symposium on Circuits and Systems, 2004. MWSCAS'04.2004.
73. Hough PV. Machine analysis of bubble chamber pictures. Paper presented at: Conf. Proc.1959.
74. Shapiro LG, Stockman GC. *Computer vision.* Prentice Hall; 2001.
75. Ballard D. Generalising the Hough Transform to detect arbitary patterns. *Pattern Recognition.* 1981;13.
76. Duda RO, Hart PE. Use of the Hough transformation to detect lines and curves in pictures. *Commun ACM.* 1972;15(1):11–15.
77. Liu H, Qian Y, Lin S. Detecting Persons using Hough Circle Transform in Surveillance Video. Paper presented at: VISAPP (2)2010.

78. Mitra J, Chandra A, Halder T. Peak trekking of hierarchy mountain for the detection of cerebral aneurysm using modified Hough circle transform. *ELCVIA Electronic Letters on Computer Vision and Image Analysis.* 2013;12(1):57-84.
79. Kanopoulos N, Vasanthavada N, Baker RL. Design of an image edge detection filter using the Sobel operator. *IEEE Journal of solid-state circuits.* 1988;23(2):358-367.
80. Canny J. A computational approach to edge detection. *IEEE Transactions on pattern analysis and machine intelligence.* 1986. (6):679-698.
81. Harris CG, Stephens M. A combined corner and edge detector. Paper presented at: Alvey vision conference1988.
82. 1w2w3y. Own work. In: circle CHtofpoa, ed. Creative Commons: ShareAlike 3.0 Unported; 2014:Circle Hough transform of four points on a circle.
83. Xie Y, Ji Q. A new efficient ellipse detection method. Paper presented at: Object recognition supported by user interaction for service robots2002.
84. Mildenberger P, Eichelberg M, Martin E. Introduction to the DICOM standard. *European radiology.* 2002;12(4):920-927.
85. Li XA, Tai A, Arthur DW, et al. Variability of Target and Normal Structure Delineation for Breast Cancer Radiotherapy: An RTOG Multi-Institutional and Multiobserver Study. *International Journal of Radiation Oncology*Biology*Physics.* 2009;73(3):944-951.
86. Barrett S. Raters and examinations. In: *Applied Rasch Measurement: A Book of Exemplars.* Springer; 2005:159-177.
87. Chollet F. keras. In. 2015.
88. Kim H-S, Kang W-S, Shin J-I, Park S-H. Face detection using template matching and ellipse fitting. *IEICE TRANSACTIONS on Information and Systems.* 2000;83(11):2008-2011.
89. Porrill J. Fitting ellipses and predicting confidence envelopes using a bias corrected Kalman filter. *Image and vision computing.* 1990;8(1):37-41.
90. Nguyen H-T, Caplier A. Elliptical local binary patterns for face recognition. Paper presented at: Asian conference on computer vision2012.
91. Kestin LL, Sharpe MB, Frazier RC, et al. Intensity modulation to improve dose uniformity with tangential breast radiotherapy: Initial clinical experience. *International Journal of Radiation Oncology*Biology*Physics.* 2000;48(5):1559-1568.
92. Lo Y-C, Yasuda G, Fitzgerald TJ, Urie MM. Intensity modulation for breast treatment using static multi-leaf collimators. *International Journal of Radiation Oncology* Biology* Physics.* 2000;46(1):187-194.
93. Evans PM, Donovan EM, Partridge M, et al. The delivery of intensity modulated radiotherapy to the breast using multiple static fields. *Radiotherapy and Oncology.* 2000;57(1):79-89.
94. Hansen VN, Evans PM, Shentall GS, Helyer SJ, Yarnold JR, Swindell W. Dosimetric evaluation of compensation in radiotherapy of the breast: MLC intensity modulation and physical compensators. *Radiotherapy and oncology.* 1997;42(3):249-256.
95. Caudell JJ, Jennifer F, Keene KS, et al. A dosimetric comparison of electronic compensation, conventional intensity modulated radiotherapy, and tomotherapy in patients with early-stage carcinoma of the left breast. *International Journal of Radiation Oncology* Biology* Physics.* 2007;68(5):1505-1511.
96. Oelfke U, Bortfeld T. Inverse planning for photon and proton beams. *Medical Dosimetry.* 2001;26(2):113-124.
97. Zygmanski P, Kung J. Method of identifying dynamic multileaf collimator irradiation that is highly sensitive to a systematic MLC calibration error. *Medical physics.* 2001;28(11):2220-2226.

98. Zygmanski P, Rosca F, Kadam D, et al. Determination of depth and field size dependence of multileaf collimator transmission in intensity-modulated radiation therapy beams. *Journal of Applied Clinical Medical Physics.* 2007;8(4):76-95.
99. Beer A. Bestimmung der absorption des rothen lichts in farbigen flussigkeiten. *Ann Physik.* 1852;162:78-88.
100. Bouguer P. *Essai d'optique sur la gradation de la lumière.* chez Claude Jombert, ruë S. Jacques, au coin de la ruë des Mathurins, à l …; 1729.
101. Lambert J-H. *JH Lambert,... Photometria, sive de Mensura et gradibus luminis, colorum et umbrae.* sumptibus viduae E. Klett; 1760.
102. Wu Q, Mohan R, Morris M, Lauve A, Schmidt-Ullrich R. Simultaneous integrated boost intensity-modulated radiotherapy for locally advanced head-and-neck squamous cell carcinomas. I: dosimetric results. *International Journal of Radiation Oncology* Biology* Physics.* 2003;56(2):573-585.
103. Helal A, Omar A. Homogeneity index: effective tool for evaluation of 3DCRT. *Pan Arab Journal of Oncology.* 2015;8(2):20-24.
104. Petrova D, Smickovska S, Lazarevska E. Conformity index and homogeneity index of the postoperative whole breast radiotherapy. *Open access Macedonian journal of medical sciences.* 2017;5(6):736.
105. Taylor CW, Povall JM, McGale P, et al. Cardiac dose from tangential breast cancer radiotherapy in the year 2006. *International Journal of Radiation Oncology* Biology* Physics.* 2008;72(2):501-507.
106. Giraud P, Cosset J-M. Radiation toxicity to the heart: physiopathology and clinical data. *Bulletin du cancer.* 2004;91(3):147-153.
107. Kahán Z, Csenki M, Varga Z, et al. The risk of early and late lung sequelae after conformal radiotherapy in breast cancer patients. *International Journal of Radiation Oncology* Biology* Physics.* 2007;68(3):673-681.
108. Neal A, Torr M, Helyer S, Yarnold J. Correlation of breast dose heterogeneity with breast size using 3D CT planning and dose-volume histograms. *Radiotherapy and Oncology.* 1995;34(3):210-218.
109. Cressie N, Whitford H. How to use the two sample t-test. *Biometrical Journal.* 1986;28(2):131-148.
110. Valdes G, Simone II CB, Chen J, et al. Clinical decision support of radiotherapy treatment planning: a data-driven machine learning strategy for patient-specific dosimetric decision making. *Radiotherapy and Oncology.* 2017;125(3):392-397.
111. El Naqa I, Li R, Murphy MJ. Machine learning in radiation oncology. *Theory Appl.* 2015.57-70.
112. Fan J, Wang J, Chen Z, Hu C, Zhang Z, Hu W. Automatic treatment planning based on three-dimensional dose distribution predicted from deep learning technique. *Medical physics.* 2019;46(1):370-381.
113. McNabb E, Wong R, Noseworthy MD. Differentiating platinum coated brachytherapy seeds and gold fiducial markers with varying off-resonant frequency offsets. *Magnetic resonance imaging.* 2019;60:68-75.
114. Wang MY, Maurer Jr CR, Fitzpatrick JM. Automatic technique for localizing externally attached fiducial markers in volume images of the head. In.: Google Patents; 1998.
115. BAO N, CUI Z-m, ZHUANG J-f, KANG Y. Automatic Segmentation of Fiducial Marker Based on Sequence Characteristics. *Journal of Northeastern University (Natural Science).* 2016. (12):8.
116. Shanafelt T, Dyrbye L. Oncologist burnout: causes, consequences, and responses. *Journal of Clinical Oncology.* 2012;30(11):1235-1241.
117. Ibragimov B, Xing L. Segmentation of organs-at-risks in head and neck CT images using convolutional neural networks. *Medical physics.* 2017;44(2):547-557.

118. Sahiner B, Pezeshk A, Hadjiiski LM, et al. Deep learning in medical imaging and radiation therapy. *Medical physics.* 2019;46(1):e1-e36.